Electrical & Computer Engineering

EE 4BI6 Electrical Engineering Biomedical Capstones

McMaster University *Year 2010*

Time-Domain Approach to Microwave Imaging for Breast Cancer Detection

Yona Baskharoun

McMaster University

Time-Domain Approach to Microwave Imaging for Breast Cancer Detection

by

Yona Baskharoun

Electrical and Biomedical Engineering
Faculty Advisor: Prof. Nikolova

Electrical and Biomedical Engineering Project Report
submitted in partial fulfillment of the degree of
Bachelor of Engineering

McMaster University
Hamilton, Ontario, Canada
April 23rd, 2010

ABSTRACT

Current imaging modalities used for breast cancer detection are unreliable and insufficient for society's needs. Microwave imaging for breast cancer detection has the potential to safely and accurately detect breast tumors at a relatively low cost. The main driving force for using microwaves to detect breast tumors is the observation that, at microwave frequencies, the dielectric permittivity and the conductivity of tumors are sufficiently different from those of normal breast tissue to enable imaging and detection. This project focuses on the use of a high-speed digital oscilloscope, which has become available only recently. It can capture pulses of bandwidth up to 20 GHz in order to further examine the abilities of an ultra wideband, near-field microwave imaging system for breast cancer detection in real time-domain measurements. The Vector Network Analyzer also contains a time-domain option offering a synthesized time-domain approach. These instruments enable the time-domain measurement, rather than the more common frequency-domain measurement, of the transmitted waves that result from illuminating breast-mimicking phantoms with ultra wideband microwave pulses. The project includes the fabrication of the appropriate breast- and tumor-mimicking phantoms used in experiments. Time-domain simulations as well as two different experimental setups are performed. The dielectric properties of breast tissue and tumors, the used breast phantoms, some characteristics of the TEM horn antenna, the simulation setup and results as well as the experimental setup and results are presented.

Keywords: microwave imaging, time-domain, breast cancer detection, breast phantom, phantom fabrication

ACKNOWLEDGEMENTS

The author would like to acknowledge the help of Natalia Nikolova, PhD, for her guidance and support in most of the work performed for this report. The author would also like to thank Aastha Trehan for her help and support in many ways, and Reza Khalaj Amineh, Kaveh Moussakhani, Sadegh Dadash and Li Liu for their assistance in the numerous simulations and experiments performed.

TABLE OF CONTENTS

LIST OF FIGURES

LIST OF TABLES

NOMENCLATURE

Phantom – A fabricated substance intended to mimic the properties of some biological tissue.

Specificity – Specificity is a measure of an imaging modality's ability to discern healthy tissue.

Sensitivity – Sensitivity is a measure of an imaging modality's ability to detect a cancerous tumor.

Contrast – The factor by which one medium's dielectric properties are higher than another's.

1. INTRODUCTION

Cancer is increasingly becoming a concern around the world, not only to the patients themselves, but also to healthcare professionals who stand helpless against all the different kinds of cancer. Great amounts of funds being invested in order to find a cure for cancer; however, until any of this research proves successful, the current techniques used to contain cancerous cells and keep them from spreading highly depend on the early detection of tumors. One type of cancer that affects a great number of women is breast cancer. On one side, breast cancer is one of the more controllable and manageable forms of cancer; however, early detection still plays a crucial role in the management of the disease.

As seen in Figure 1, breast cancer accounted for 27.8% of 81,700 new cancer cases and 15.1% of 35,700 cancer deaths in females in Canada during 2009 [1], being the leading type of cancer to affect women and the second cause of cancer deaths in women. Figure 2 shows that breast cancer has maintained its leading role as the leading cause of cancer in females since 1980 while Figure 3 shows that the mortality rates due to breast cancer has decreased since then [1]. One of the main reasons behind this decrease in mortality rates due to breast cancer is the women's increased awareness of the importance of early detection of cancerous cells in the breast and their commitment to regular breast scans.

Mammography is currently the most widely clinically accepted method for breast imaging; however, there are two main drawbacks to this procedure. First, it causes discomfort to the patient because it causes painful breast compression. In addition, mammography leads to exposure to potentially harmful iodizing radiation, which could result in women being more resistant to having regular scans. Second, mammography detection has a relatively high false-negative rate (4%-34%) and false-positive rate (70%) [2]. Mammography also misses around 15% of breast cancer and has a in detecting cancers in dense breasts [3]. Ultrasound, MRI and other breast cancer detection modalities are available; however, they are either less effective or too expensive and time consuming [4]. Due to the lack of a comfortable, efficient, inexpensive and readily available imaging modality to detect breast cancer, the need for a new imaging modality to detect breast tumors has presented itself.

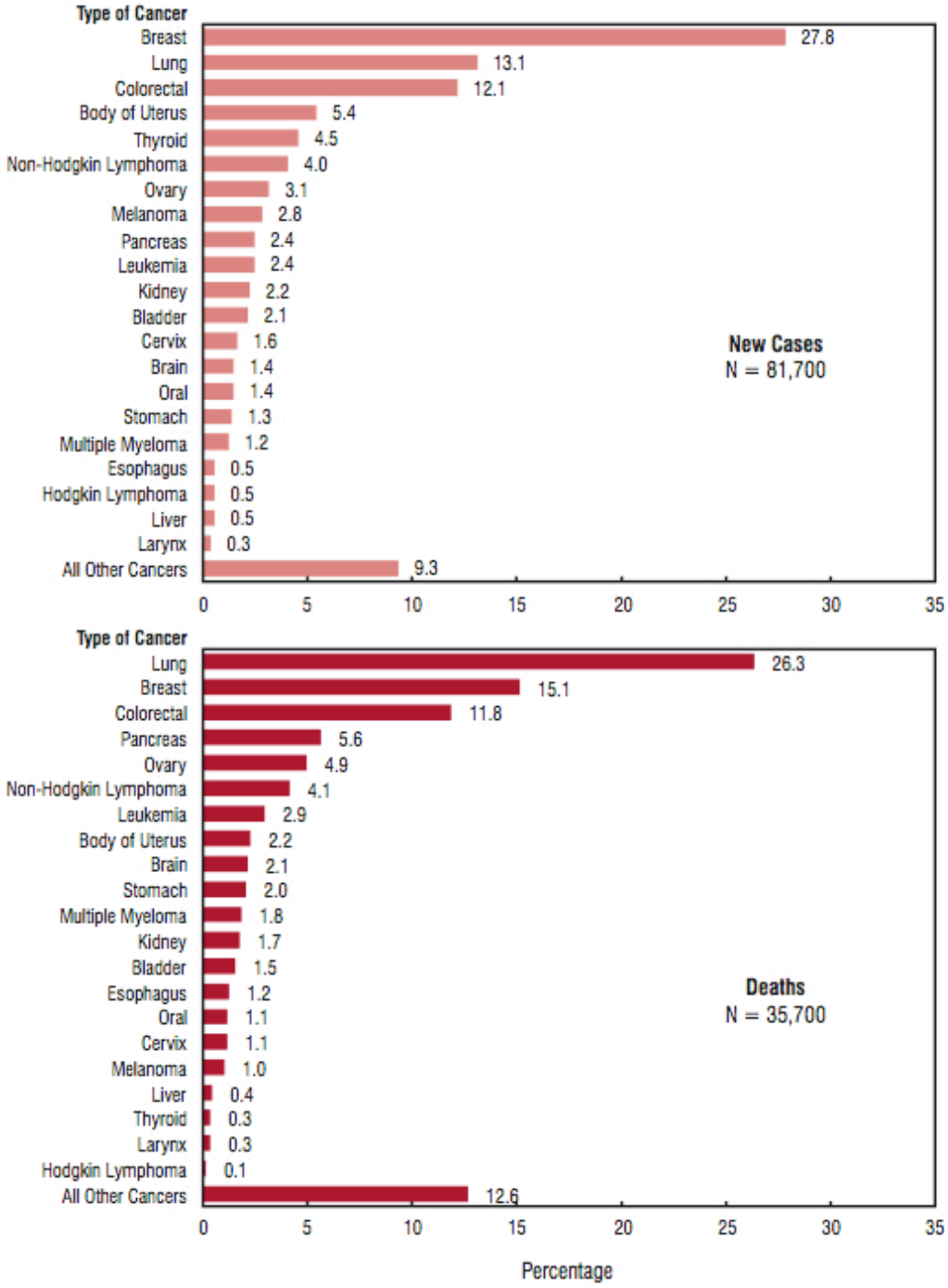

Figure 1:Percentage distribution of estimated new cases and deaths for selected cancers, females, Canada, 2009.

Source: [1]

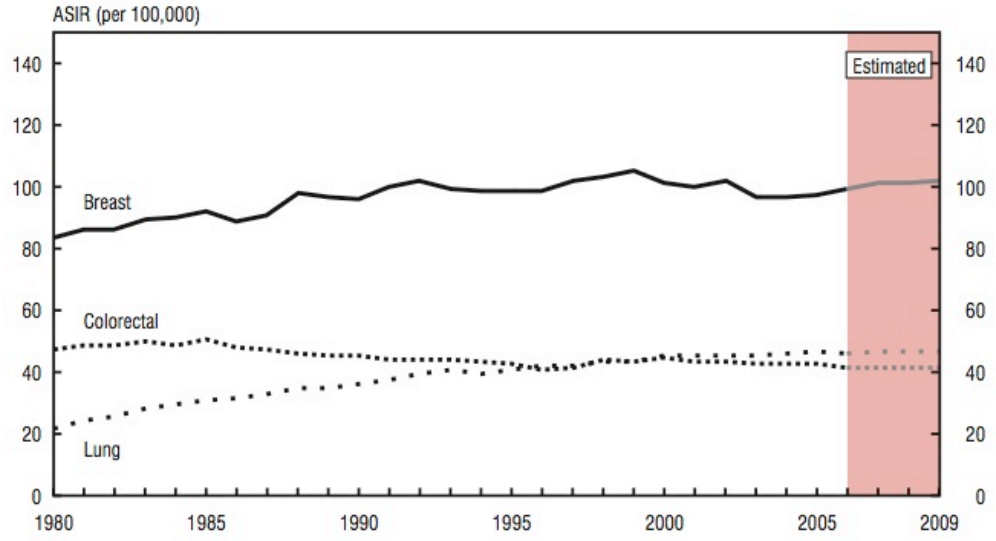

Figure 2: Age-Standardized Incidence Rates (ASIR) for selected cancers, females, Canada, 1980-2009.

Source: [1]

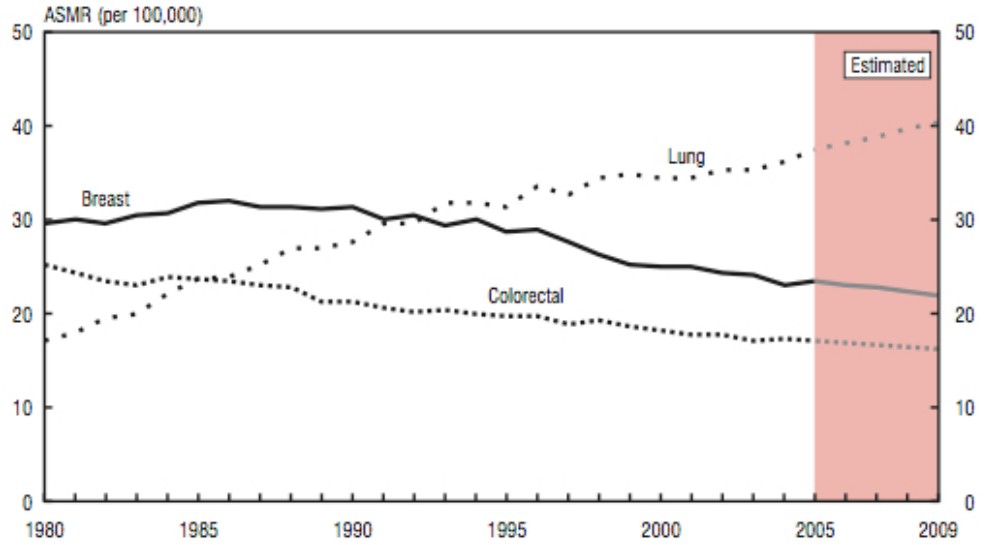

Figure 3: Age-Standardized Mortality Rates (ASMR) for selected cancers, females, Canada, 1980-2009.

Source: [1]

Microwave imaging for the purpose of breast cancer detection has the promise of avoiding the sources of discomfort or ionization as in mammography while offering sensitivity and specificity to detect small tumors. The microwave methods offer a low cost relative to methods such as the MRI and X-ray [3]. The main driving force for using

microwave imaging in breast tumor detection are the differences in the electrical properties of malignant tumors, benign tumors and normal breast tissue. It has been observed that at microwave frequencies, the dielectric permittivity and the conductivity of tumors are sufficiently different from those of normal breast tissue to enable imaging [4]. In order to detect breast tumors using microwave imaging techniques, the region of interest is illuminated with microwaves. Due to the difference in electrical properties between normal breast tissue and tumors, the microwaves are transmitted or reflected differently in the different media. The receive antenna can range from an array of many antennas to a single detection antenna. However, with the use of one receiver antenna the transmit antenna is moved to different positions to obtain results at various locations. Therefore, it is possible to create an image showing the location of the tumor by measuring the resultant transmitted or reflected energy.

Microwave detection of breast cancer, although promising, is yet to be introduced into clinical practice. This indicates a great possibility for enhancements and optimization. One of the possible sources of error in the image formation of the scatterer via time-domain techniques is that responses measured in the frequency-domain are converted into time-domain via inverse Fourier transform to be used in the image formation algorithm [5]. Information about tumor presence and characterization could be extracted directly from the time domain scatter of the ultra wideband microwave in the time domain [6] to possibly yield more accurate detection.

The main objective of this project is to use a recently introduced digital oscilloscope that can capture pulses of bandwidth up to 20GHz in order to further examine the abilities of an ultra wideband, near-field microwave imaging system for breast cancer detection in the time-domain. This oscilloscope will enable the time-domain measurement of transmitted waves that result from illuminating breast-mimicking phantoms with ultra wideband microwave pulses. It may be possible to extract direct and more accurate information about tumor presence and characteristics from the time domain UWB microwave measurements. Such a study will be able to determine whether sufficient information, by which an early stage tumor may be detected, can be obtained from time-domain measurements.

There are three main parts to this project. The first part is simulating the actual experiment using a time-domain electromagnetic simulator. The second part is the fabrication of the necessary phantoms that mimic breast tissue, mainly fat, and tumor permittivity and conductivity. The third part is performing the time-domain measurements using two TEM horn antennas and the phantoms fabricated. Measurements were performed using an Arbitrary Waveform Generator (AWG) to provide the input signal and a digital scope to view the transmitted pulse for real time-domain measurements. The time-domain option of a Vector Network Analyzer (VNA) is also used to perform the same measurements in a synthesized time-domain scenario (since the VNA inherently measures in the frequency domain). In both the simulations and the measurements, the time-domain transmitted signal across a phantoms with a tumor presents is compared to that without a tumor present in order to determine whether the tumor signature is sufficient for detection.

2. LITERATURE REVIEW

2.1 Electrical Properties of Beast and Tumor Tissues

As mentioned earlier, the main driving force in microwave imaging of breast tumors is the difference between the electric properties of malignant tumors, benign tumors and normal breast tissue. These include differences in the dielectric permittivity and the conductivity. It is indicated in [4] that the relative dielectric permittivity and conductivity of tissues depend on their water content. Thus, high-water-content (HWCT) tissue, such as muscle or malignant tumors, have a relative dielectric permittivity and conductivity that are around an order of magnitude higher than those of low-water-content (LWCT) tissue such as fat that is abundant in normal breast tissue [4]. However, even the highest water content biological tissue contains less than about 80% water [7]. The difference in the electrical properties result in different scattering parameters for normal breast tissue and breast tumors, which is the key to detecting tumors. One of the great challenges in determining the electric properties of normal breast tissue is in its great heterogeneity. Breast tissue is also highly patient dependent [7].

The most comprehensive data available on the electrical properties of normal, malignant and benign breast tissue can be found in [7] and [8]. [7] details the sources of

data used as well as the techniques used to measure the electrical properties of normal breast tissue, while [8] outlines those used to measure properties of cancerous tissue. The results of those studies are of more concern to this report.

The first most notable result is illustrated in Figure 4, which shows that, on average, more than 50% of the breast is composed of adipose tissue (or fat). Thus the use of fat-mimicking phantoms in experiments is a legitimate approach to testing the ability of microwave imaging the detect breast cancer.

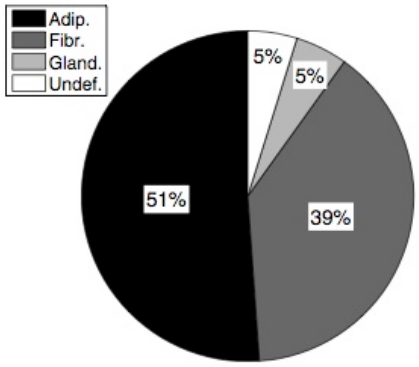

Figure 4: Distribution of dominant tissue in the breast. 'Adip.': adipose tissue, 'Fibr.': fibroconnective tissue, 'Gland.': glandular tissue, 'Undef.': undefined, which refers to cases where the tissue in the histology slide was too heterogeneous to determine the dominant type.

Source: [7]

Results were obtained for low-water-content tissue, i.e adipose tissue and high-water content tissue in [7], while [8] showed results for a random normal tissue sample and a cancerous tissue sample for the frequency range of 0 to 20 GHz. Those results are shown in Figure 5, Figure 6 and Figure 7 below.

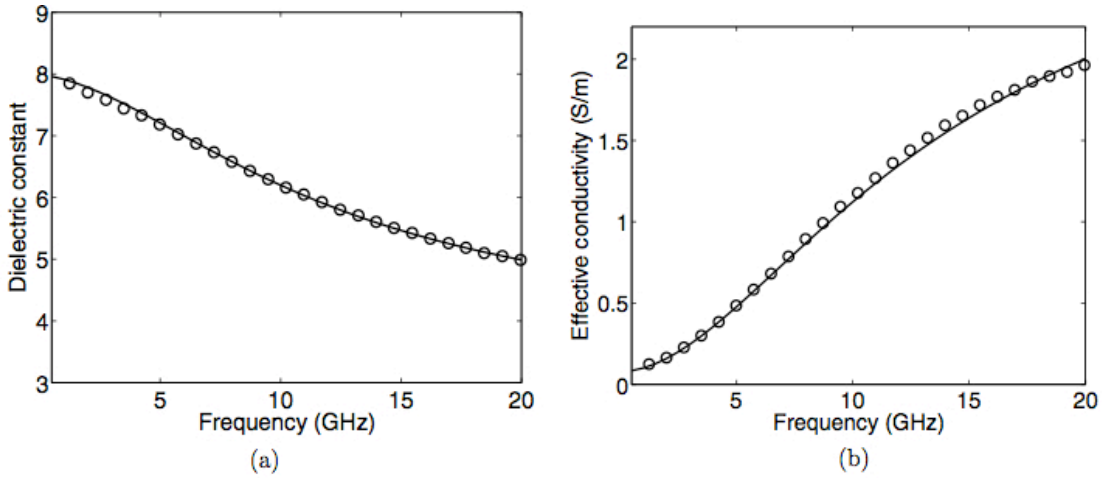

Figure 5: Example of good quality fit for a low-water-content sample. (a)Dielectric constant as a function of frequency, (b) Effective conductivity as a function of frequency.o: measured data, solid line: Cole–Cole fit.

Source: [7]

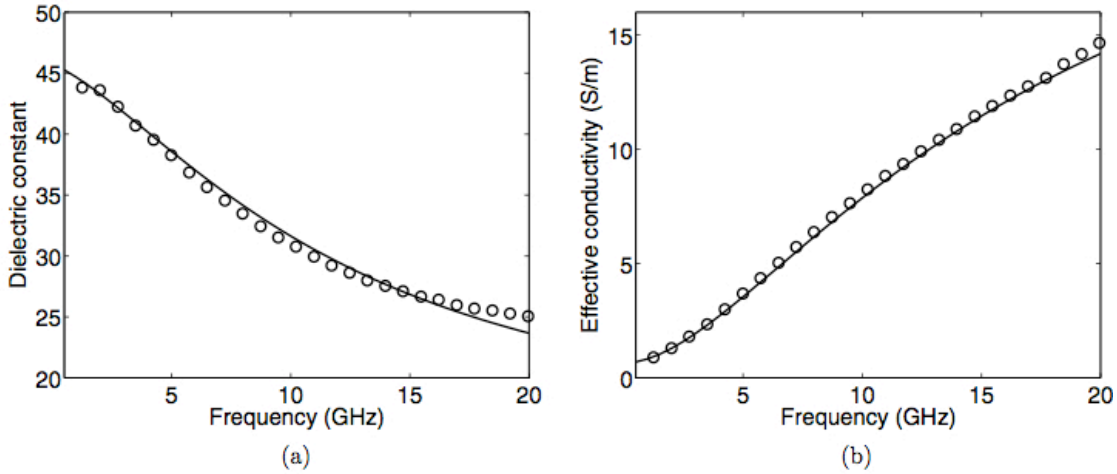

Figure 6: Example of good quality fit for a high-water-content sample. (a)Dielectric constant as a function of frequency, (b) Effective conductivity as a function of frequency.o: measured data, solid line: Cole–Cole fit.

Source: [7]

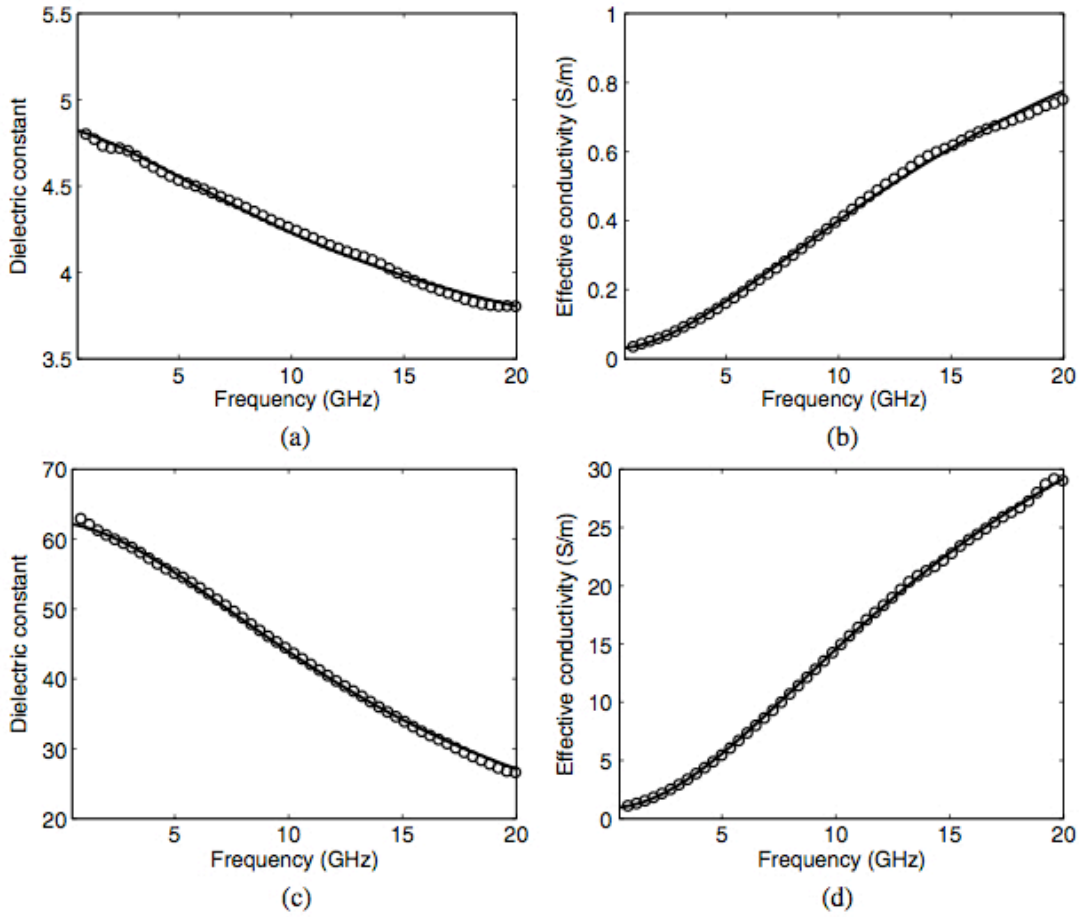

Figure 7: Examples of Cole–Cole fits to two representative experimental data sets. (a)Dielectric constant and (b) Effective conductivity as a function of frequency for a normal sample (c) Dielectric Constant and (d) Effective conductivity as a function of frequency for a cancer tissue sample.

Source: [8]

Tissue	$\varepsilon'(\omega)$	σ_{eff} (S/m)
LWCT	5 - 8	0.2 - 2
HWCT	25 - 45	1 - 15
Malignant	25 - 65	1 - 30

Table 1: Summary of dielectric properties of different breast tissue.

From the results summarized in Table 1, it is clear that the dielectric properties of adipose tissue, the tissue most abundant in the breast, is significantly different from those of malignant tissue to enable accurate detection of breast cancer. This contrast in dielectric properties between normal and cancerous breast tissue is much higher than the contrast in many other breast imaging modalities [3]. There results present one of the

various reasons behind which microwave imaging for breast cancer detection has the potential of offering the sensitivity and specificity that other modalities are yet to attain.

2.2 Confocal Microwave Imaging (CMI) for Breast Cancer Detection

The Confocal Microwave Imaging (CMI) system for breast cancer detection has been developed by the group in [2] and [9]. Similar to underground radar techniques, the scanning the breast to detect tumors using the CMI system involves illuminating the breast with an UWB pulse and measuring the backscatter to localize the tumor (scatterer). The group investigates planar and cylindrical models for breast tumor detection. The planar orientation is more relevant to this project and will therefore be discussed in more detail.

For the planar configuration, the breast is modeled as a half-space of heterogeneous breast tissue bounded by a 2 mm thick layer of skin with values $\varepsilon_r = 36$ and $\sigma = 4$ S/m. The breast is modeled as a 10 cm by 10 cm by 5.5 cm rectangular prism with the dielectric properties of a normal beast tissue with values $\varepsilon_r = 9$ and $\sigma = 0.4$ S/m with ±10% variations. The tumor is 6 mm in diameter and is located at a minimum distance of 3cm below the skin. A 2 cm in length bowtie antenna is placed directly on the skin and used to scan the breast at different locations as seen in Figure 8 [2] At each position the bowtie antenna is excited with an ultra-wideband differentiated Gaussian pulse of the form

$$V(t) = V_o(t - t_o)e^{-(t-t_o)^2/\tau^2} \qquad (1)$$

where V_o is used to adjust the amplitude, τ = 62.5 ps, $t_o = 4\tau$ [2]. For the planar configuration, the current at the antenna feed is recorded containing the backscatter from the breast [2]. It is important to note that this system setup and its results are all simulated with no actual measurements.

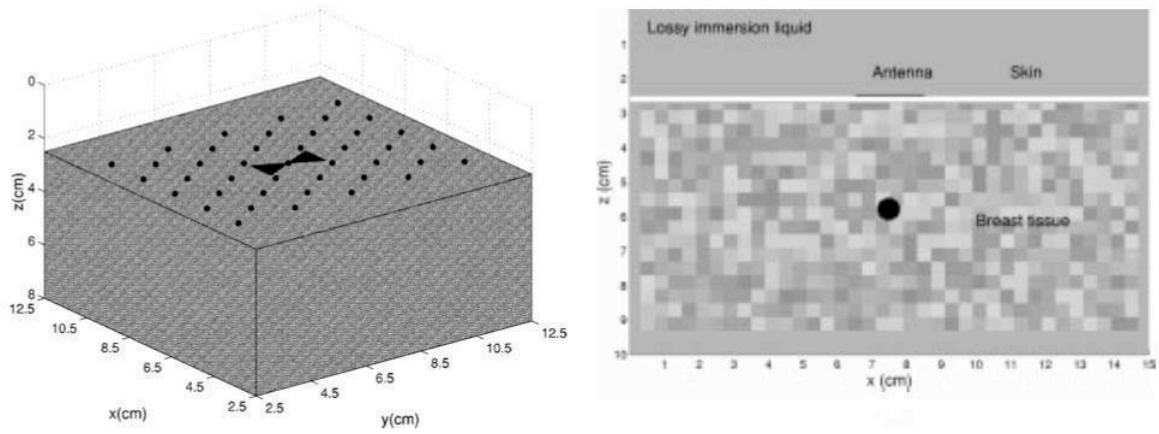

Figure 8: a) Arrangement of antenna array for planar system. b) Model of the planar system where the antenna is backed by an impedance matching layer of lossy liquid similar to breast tissue.

Source: [2]

The image formation process of the results of this system has various steps. Calibration is first conducted to remove the incident pulse (since the same antenna is used to transmit and receive) and to remove skin backscatter content, referred to as the early-content of the signal. This is performed by subtracting the average of the returns at each antenna in a given row from each return in that row. Integration is then performed to have a maximum, rather than a zero, at the center point of the signal to allow for non-destructive addition of local maxima in straightforward time-shifting in preparation for the synthetic focusing process. Compensation for path loss is then applied to the signal to correct for the reduction in signal strength due to propagation through lossy breast tissue [2]. The final processed signal is shown in Figure 9 below.

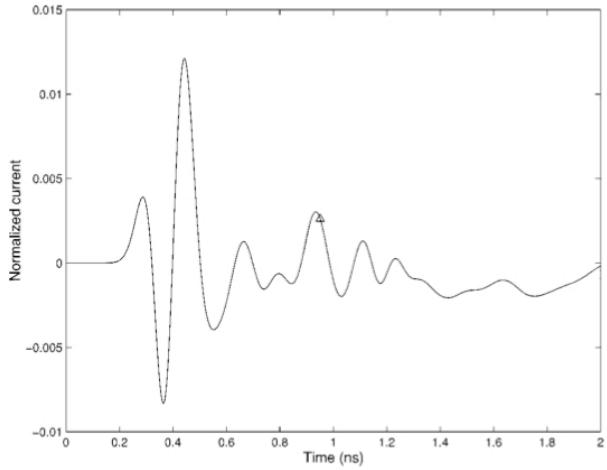

Figure 9: Final processed signal. The triangle marks the tumor response.

Source: [2]

Finally, the image is reconstructed using synthetic focusing of the processed signals. Synthetic focusing is performed as seen in Figure 10, by first computing the distances from each antenna to the focal point and converting them into a time delays that are used to identify the contribution of each signal. All contributions are summed and squared and assigned to the pixel value at the focal point to result in a corresponding intensity at each point on 2D images of the different cross-sections shown in Figure 11 [2].

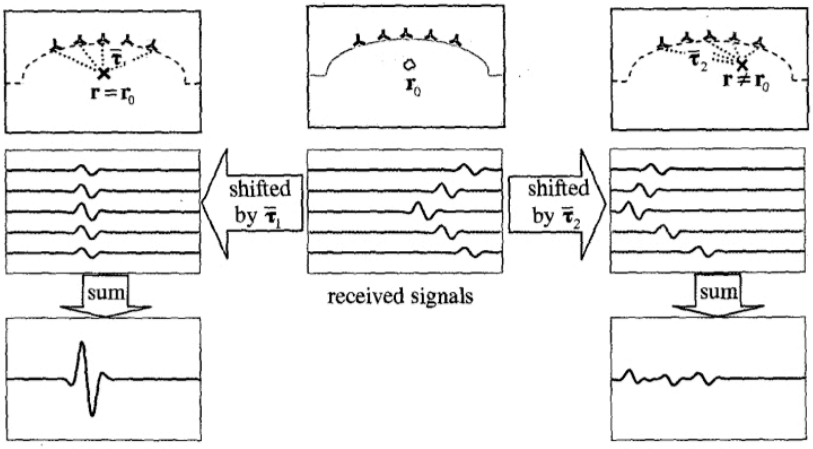

Figure 10: Synthetic Focusing: when the scatterer is at the focal point, the sum of the signals is constructive yielding a higher intensity than when the scatterer is not at the focal point and destructive sum with lower intensity.

Source: [10]

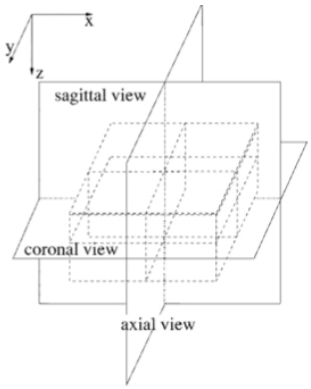

Figure 11: Image planes for the planar system.

Source: [2]

The resultant images of planar breast models with a tumor are shown in Figure 12 for the three planes mentioned above. The figures are normalized to the maximum of the reconstructed data set [2]. The results show that the CMI is a feasible system to detect breast tumors with the main limitations being the effect of various sources of noise and artifacts on the synthetic focusing algorithm.

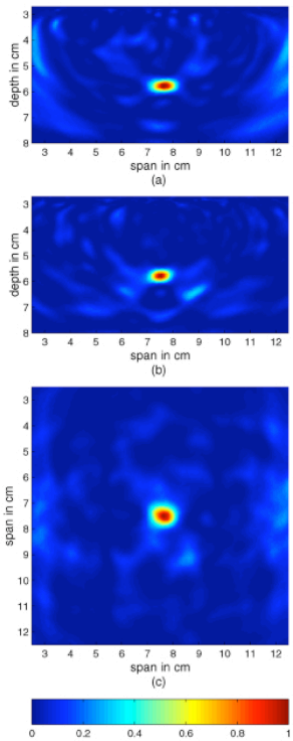

Figure 12: 3D reconstructed image in the three planes: a) axial, b) sagittal, c) coronal. Source: [2]

The other system being currently studied to detect breast tumors is the Tissue Sensing Adaptive Radar (TSAR) system for breast cancer detection developed by the group in [5] [11] and [12]. The TSAR system senses all the reflections in the region of interest and uses the resulting information for image reconstruction algorithms [11]. [5], [11] and [12] show experimental and simulation setups and results of this system. The image reconstruction algorithms are similar to those used in the CMI system discussed above.

Both the CMI and TSAR systems show encouraging results; however, they both indicate that time-domain signals are required for the image reconstruction algorithm and that the use of inverse chirp-z transform to convert the signal to time-domain is the first part to every image reconstruction algorithm [2] [5]. Therefore, the ability to measure the signals directly in the time-domain would not only decrease computational time and effort, but would also eliminate any errors that result from the use of the inverse chirp-z transform to obtain the required time-domain signals. It is here that this project hopes to improve upon previous work and present preliminary experimental and simulated results

of direct time-domain recording of signals in a microwave imaging system for breast cancer detection.

3. Statement of Problem and Methodology of Solution

Prior to outlining the experimental setup used in performing time-domain measurements in this project, it is necessary to detail the various parts of the experiment. That includes a TEM horn antenna to transmit and receive microwaves, breast and tumor mimicking phantoms and other equipment used to generate and record the time-domain signals.

3.1 TEM Horn Antenna

The antenna in [13] and [14] has been designed specifically for the purpose of performing measurements for ultra wideband microwave imaging for breast cancer detection. This TEM horn antenna is used in the experiments performed in this project. This antenna has three main advantages. Firstly, this antenna directs all of the radiated power through the front aperture of the antenna, and consequently through the tissue. Secondly, this antenna efficiently eliminates outside electromagnetic interference. Thirdly, this antenna can operate in direct contact with the body and thus eliminates to need of a coupling liquid [13], which has many disadvantages presented [15].

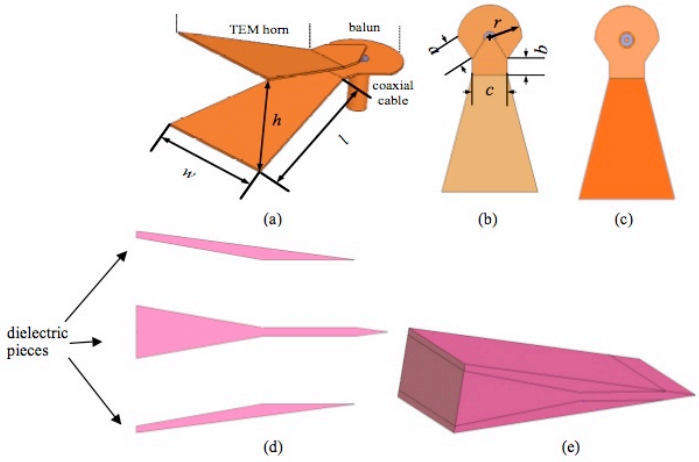

Figure 13: (a) The TEM horn with the coaxial feed and the balun. (b) Top view of the TEM horn. (c) Bottom view of the TEM horn. (d) Cross-section view of the three solid dielectric antenna pieces. (e) After mounting the copper plates of the TEM horn on the middle dielectric piece, all three dielectric parts are glued together.

Source: [14]

The antenna consists of a TEM horn antenna embedded in a solid dielectric medium as seen in Figure 13. Figure 13 (a) shows the two plates of the TEM horn, which are fed by coaxial cables via a balun. Figure 13 (d) shows the cross section of the solid dielectric medium. The dielectric medium has a relative permittivity of 10 and tanδ<0.002 in the frequency range from 1 to 10 GHz [14].

In order to efficiently eliminate outside electromagnetic interference, the antenna is shielded with copper sheets and an absorbing sheet as seen in Figure 14 (a). The design parameters shown in Figure 14 have been optimized so that the antenna is matched to a 50-Ω coaxial cable in the whole UWB frequency range. Table 2 shows the design parameters of the antenna used.

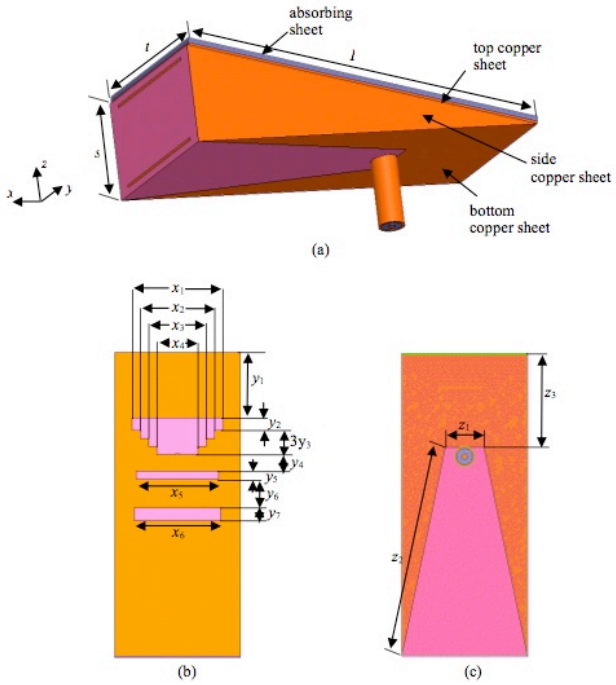

Figure 14: (a) The TEM horn placed in a dielectric medium with relative permittivity of 10 with copper sheets on all outer surfaces except the front aperture and a microwave absorbing sheet on the top surface. (b) The copper sheet pattern on the top surface. (c) The copper sheet pattern on the bottom surface.

Source: [13]

Parameter	Value (mm)	Parameter	Value (mm)
l	38	x_4	10
w	24	x_5	20
h	16	x_6	21
a	8	y_1	16
b	5	y_2	3
c	11	y_3	2
r	11	y_4	4
L	74	y_5	2
s	19	y_6	7
t	30	y_7	3
x_1	22	z_1	9
x_2	18	z_2	52
x_3	14	z_3	23

Table 2: Design parameters for the antenna.

Source: [13]

The antenna characterization includes return loss, total efficiency, near-field directivity, fidelity, and group velocity can be found in [14]. The most relevant time-domain characterization of the antenna is fidelity. Fidelity is calculated as the cross-correlation between the input signal's template and the output E-field waveforms [14]. Figure 15 shows the computed fidelity of the antenna as a function of the distance from the antenna aperture.

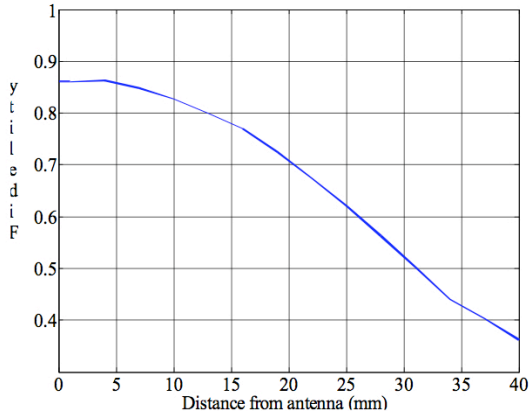

Figure 15: Simulated fidelity versus the distance from the center of the antenna aperture and along the aperture normal.

Source: [14]

It is important to note here than, like other horn antennas, the antenna used in the experiments does not work efficiently around DC. The lower frequency limit for this

antenna is 3 GHz and the upper limit is 10 GHz. Thus, the antennas do no transmit or receive the frequency components of pulses that are below 3 GHz and above 10 GHz.

3.2 Breast and Tumor Mimicking Phantoms

Physical phantoms are used to aid in performing the necessary experiments. The physical phantoms should mimic the electric field distribution and relative heating patterns of the real breast tissue when excited with an electromagnetic source [16]. A phantom recipe typically mimics only a single kind of human tissue. Therefore, it exhibits a homogenous distribution of electrical and thermal properties specific to the mimicked tissue [16]. Phantoms mimic the E-field distribution and relative heating patterns of the actual tissue in the presence of an electromagnetic source. They are mechanically stable, non-toxic, easy to maintain, and fabricated at a relatively low cost. The recipes used to fabricate the phantoms are taken from chapter 3 of [16]. The different phantom recipes mimic fat, fibro-glandular, muscle and tumor tissue. The main ingredients of the phantoms are water, glycerin and Polyethylene Powder (PEP). The different recipes can be found in Appendix I. It is important to note that the properties of the fabricated phantoms are measured using a dielectric probe that records the frequency dependant variables ε'(ω) and ε"(ω). ε'(ω) is the relative permittivity of the medium while the effective conductivity is calculated using ε"(ω) an in (2). The electrical properties of the phantoms, mainly permittivity and conductivity, will be presented later on in this report in the detailed explanation of the experiments performed.

$$\sigma_{eff} = \omega \varepsilon_o \varepsilon''(\omega) \qquad (2)$$

3.3 Other Instrumentation Used in the Experimental Setup

- Arbitrary Waveform Generator (AWG): Tektronix AWG7102 [17]
- Scope: Tektronix DSA72004B Digital Serial Analyzer [17]
- Vector Network Analyzer: Agilent Technologies E8363B PNA Network Analyzer [18]
- Amplifiers: Mini-Circuits Amplifier ZX60-14012L-S [19]

4. SIMULATION DESIGN PROCEDURE

4.1 Geometry and Setup

Simulations were performed using QuickWave-3D (QW3D) [20], an electromagnetic simulator based on finite-difference-time-domain (FDTD) method. The simulation geometry and setup used in the simulation resemble those used in the experiments. The simulation geometry can be seen in Figure 16. The rectangular prism simulates compressed breast tissue with the electrical properties of fat, $\varepsilon_r = 6$ and $\sigma = 0.2$ S/m. The dimensions of the rectangular prism are 50mm by 20mm by 50mm in the x, y and z directions respectively. The surrounding medium is air. The tumors used have $\varepsilon_r = 30$ and $\sigma = 3$ S/m resulting in a 5:1 contrast in permittivity and 15:1 contrast in conductivity.

The diameter of the inserted tumor simulant is varied and the presence of multiple tumors is also examined. Figure 17 shows the geometry of the simulation setup when two tumors are inserted. In order to maintain a certain amount of symmetry in the simulation geometry several points were always ensured. In the presence of one tumor, its center is always at the center of the prism and only the diameter is altered. In the presence of two tumors, they are always placed at equal distances from the y-axis. The diameters of both tumors are always equal. The distance between the tumors is reported as the distance between the sides of the spheres rather than their centers. Although the actual size of the phantom is around 10cm by 3cm by 10cm (in the x, y and z directions, respectively), simulating such dimensions would require a lot of computational effort and memory. Therefore, as long as the dimensions are significantly larger than the wavelength of the used signals, it has been decided that the chosen simulated dimensions will suffice for our purpose. An absorbing boundary box is used to simulate infinite space.

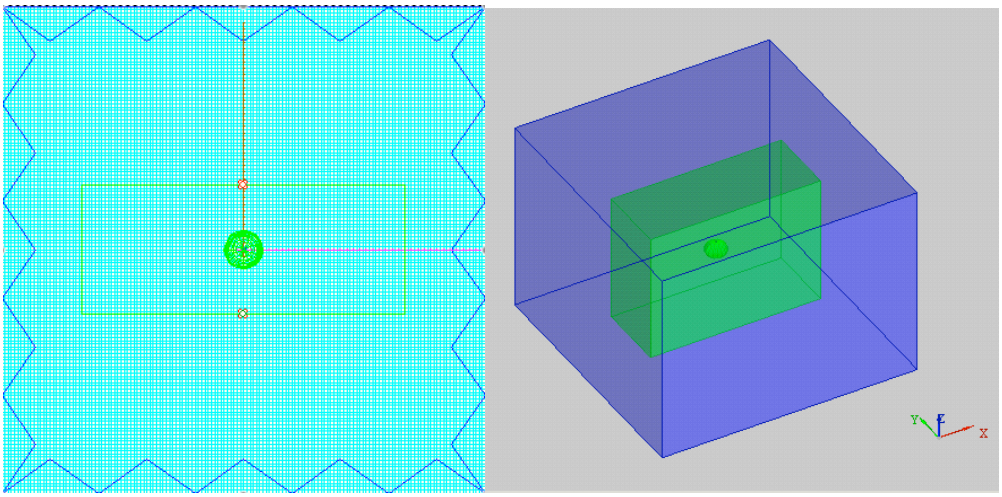

(a) (b)

Figure 16: a) 2D view of simulation geometry with one tumor. b) 3D view of simulation geometry with axes orientation.

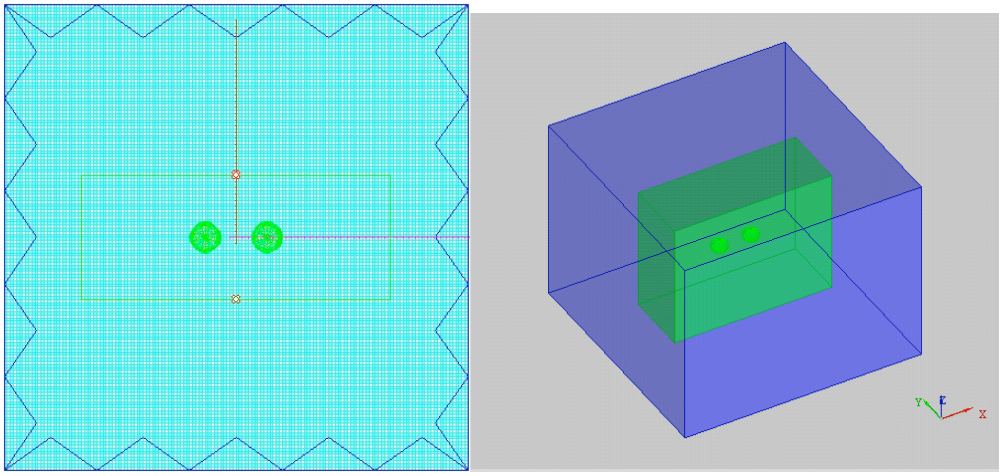

(a) (b)

Figure 17: a) 2D view of simulation setup with two tumors. b) 3D simulation setup with two tumors.

The top point is an excitation point source and the bottom one is a probe. The source point is a current source and the excitation pulse has been chosen as an E_z field component whose waveform is a Gaussian pulse with bandwidth from 3GHz to 10 GHz. At each point, it has been determined that measuring the time-domain voltage waveform at the probe yields the most accurate results.

The source and the probe are directly opposite to each other and are moved simultaneously in the x and y directions to perform a 2D scan, This setup is to simulate

two antennas facing each other at both sides of the phantom, where one antenna excites and the other one records the transmitted signal. The simulation at each point is performed twice, once without the presence of the tumor and one with the tumor present. It is worth noting here that the *x*-direction is zero at the center of the prism and goes to ±25 mm in the opposite directions. QuickWave [20] does not contain a parameter sweep option in which the *x* and *y* locations of the probe and the source can be swept in a single simulation; therefore, the probe and the source were manually placed at 1 mm intervals in the positive half of the *x* direction only from $x = 0$ to $x = 13$ mm then at wider intervals after $x = 13$ mm namely at $x = 15$, 17, 20, and 25 mm. This was determined to be sufficient due to the symmetric nature of the simulation geometry. This also limits the locations of the tumors to ones that maintain this symmetry to some extent.

4.2 Image Formation

At every *x* location, the time-domain voltage waveforms at the probe with and without a tumor simulant present are saved. Using a MATLAB algorithm, a sample of which is presented in Appendix II-A, the energy of each signal is obtained by simply integrating it. The tumor signature is determined by subtracting the energy of the simulation result without a tumor from that with a tumor. For the *x* locations with no corresponding simulations, the result of the previous point (in the negative *x* direction) is used. Thus, an intensity level at every point is obtained and the intensity at every point is plotted to produce an image in the presence of one tumor (due to symmetry in all directions) or a simple plot in the presence of two tumors (due to limited symmetry).

5. EXPERIMENTAL DESIGN PROCEDURE

The experimental setups are similar to the simulation setup. An antenna is placed on opposite sides of the phantom; one antenna transmits and the other one receives the signal. The antennas are connected to the AWG/scope/VNA using 50 Ω coaxial cables. The phantoms used for measurements are LWCT phantoms and HWCT phantoms. Results are only obtained for the LWCT phantoms while the HWCT measurement only

aims to show the difficulty of detecting a transmitted signal in those very high loss phantoms.

5.1 Phantoms

As mentioned earlier, the phantoms were fabricated using recipes in chapter 3 of [16] with some alterations in the Malignant-1 recipe for tumor phantoms. The phantom recipes can be found in Appendix I. The different recipes are for the different tissue types present in breasts. HWCT-1 is the recipe for highest water content healthy tissue phantom for breast phantom namely muscle. HWCT-2 is the highest water content healthy tissue inside breast phantom, namely fibro-glandular (FG) tissue. IWCT is the intermediate water content tissue phantom, same for both skin and transitional tissue. LWCT is for lowest permittivity and loss tissue phantom namely adipose fat in breast, which is the phantom mostly used in this experiment. Malignant-1 is the recipe used for tumors.

The HWCT, IWCT and LWCT phantoms are fabricated by first mixing the appropriate amounts of the liquid ingredients, DIW (de-ionized water) and glycerol (and ethylene glycol for LWCT phantoms) in a flask. The solution is then heated to 88^{o}C while being occasionally stirred. A few of drops of Bactine are then added to the hot solution and the flask is removed from the heater. The liquid is poured into a blender and the blender is switched on at the lowest speed. The powder ingredients, agar and PEP, are mixed in a container and added in very small amounts to the liquid solution as it is being stirred by the blender. When all the powder mixture is added to the solution, it becomes a homogeneous, beige-colored thick liquid. This homogeneous solution is poured into a rectangular container to act as a mould. The bubbles that are formed on the top of the solution are removed. Finally, the container is left to cool down to room temperature, and then placed in a fridge and allowed one to three days to solidify. Once the phantom has solidified, it is removed from the container, placed in a plastic bag and stored in the fridge [16]. The fabricated normal breast tissue phantoms can be seen in Figure 18.

Figure 18: Fabricated LWCT phantoms.

The Malignant-1 phantoms are made in a slightly different manner. The saline solution, made up of water and NaCl, is heated till a clear solution is formed. The saline is then added to the alginate and blended by hand. It has been determined that it is crucial to blend the mixture as much as possible otherwise most of the water will not be absorbed by the alginate forming a layer of ice around the tumor upon solidification and resulting in water inside the tumor which produces a tumor phantom with inaccurate properties. The mixture is then placed in a mold and placed in a fridge to solidify [16].

Once the phantoms have solidified, their properties are measured using the dielectric probe. The actual permittivity and conductivity of the phantoms used are measured using a single port dielectric probe. The probe is calibrated for frequency range of 3 to 10 GHz. Calibration is performed using the guidance of the calibration software available in the VNA. The probe measure when it is first exposed to air, then when it is shorted through use of a special shorting block, and finally when it is immersed in de-ionized water at a temperature of 25°C. Once the calibration is completed, the probe is placed on the surface of a phantom and a measurement is triggered manually. This measurement is repeated multiple times in order to obtain an average recording [16]. The setup used to perform measurements using the dielectric probe is shown in Figure 19. Figure 20 shows the relative permittivity and Figure 21 shows the effective conductivity across the frequency range of interest of the LWCT, HWCT-2 and two Malignant-1 phantoms. The tables that correspond to those plots can be found in Appendix III.

Figure 19: Dielectric probe setup

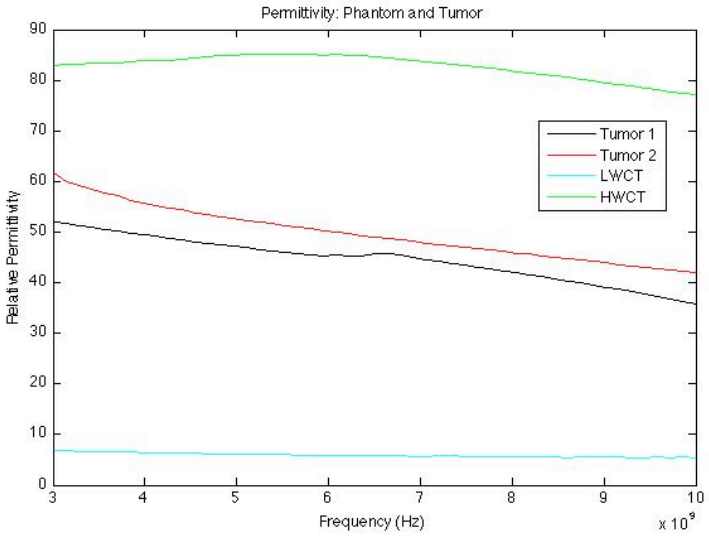

Figure 20: Measured permittivity of fabricated LWCT, HWCT and two tumors.

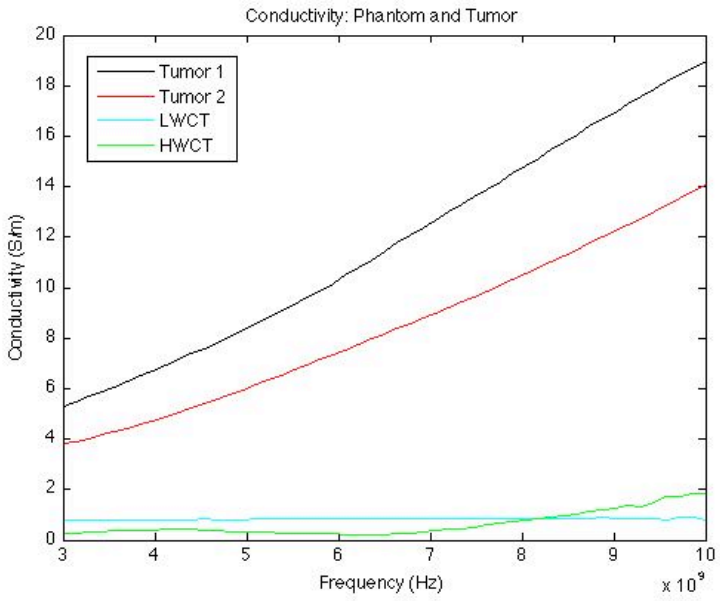

Figure 21: Conductivity of fabricated LWCT, HWCT and two tumors.

Upon comparisons with the dielectric properties of normal breast tissue presented above, it was determined that those phantoms sufficiently mimic real breast tissue and tumor properties and thus may be used in the experiments. It is worth noting that the relative permittivity of the tumor used in experiments was around 50 while that of the tumor used in simulations in 30. This only increases the permittivity contrast in the experiment setup to overcome the various sources of noise and artifacts present in actual measurements; however, the results are still comparable.

The phantom size used is 16 cm by 16 cm by 3.5 cm in the in the x, y and z directions, respectively. The tumor size used is half-sphere shaped with a diameter around 4 cm. The size of the tumor was limited by the moulds available.

5.2 Experimental Setup Using the AWG and the Scope

In this setup, the AWG is used to supply the input excitation signal to the transmit antenna, and the digital scope is used is record the transmitted signal at the receive antenna. The general setup of the experiment can be seen in Figure 22. The AWG and the scope can sample up to 20 Gs/s and are therefore suitable for this application. The input pulse is supplied to the transmit antenna via the AWG.

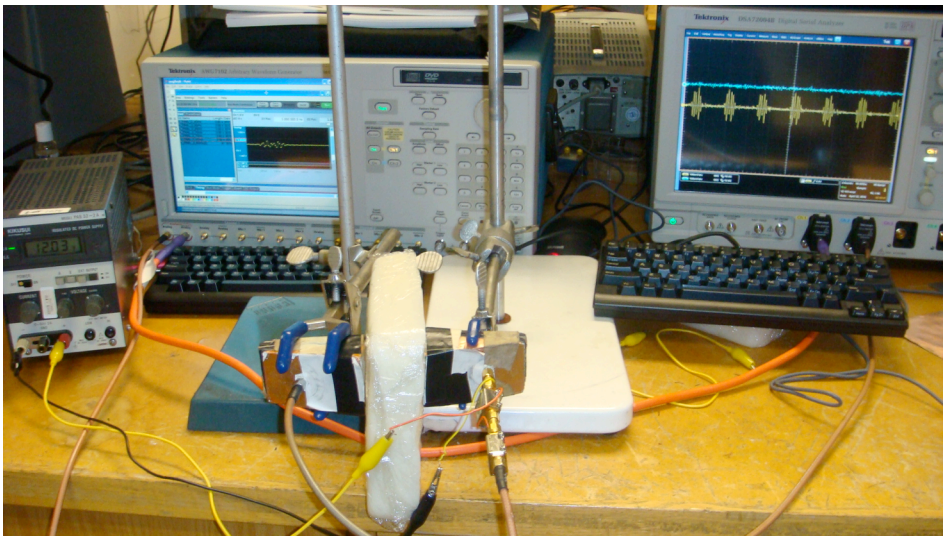

Figure 22: Experimental setup using the AWG and the scope.

The desired signal is in turn supplied to the AWG using a signal defined using MATLAB. The MATLAB code used to generate this input signal can be seen in Appendix II-B. The input is a sine modulated differentiated Gaussian pulse defined by equation (3) where V_o is used to control the magnitude and set to 5×10^9 V, $t_o = 5\tau$ and τ is used to change the frequency bandwidth of the pulse and set to 190.52 ps. It is crucial to note that is was necessary to define the time step in the MATLAB algorithm to be 0.05 ns, which is equal to 1/(20 GHz) which is the sampling frequency of the AWG. The resultant signal is shown in Figure 23 and Figure 24. This signal does not look as accurate as one would hope, however, through the filtering caused the AWG, the scope and the antennas, this signal is ideal for this application as seen later on in this report. The frequency bandwidth of the signal is in the desired range of 3 GHz to 9 GHz.

$$V(t) = V_o(t - t_o)e^{-(t-t_o)^2/\tau^2} \qquad (3)$$

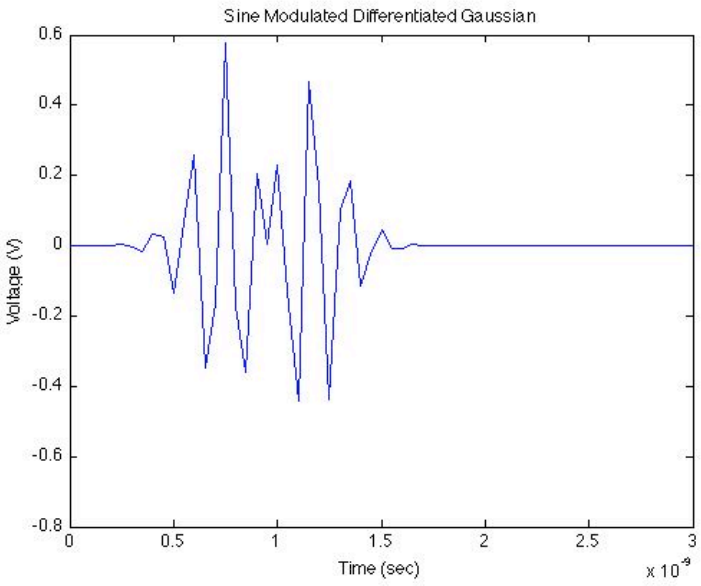

Figure 23: Input signal generated using MATLAB.

This signal does not look as accurate as one would hope, however, through the filtering caused the AWG, the scope and the antennas, this signal is ideal for this purpose as seen later in this report.

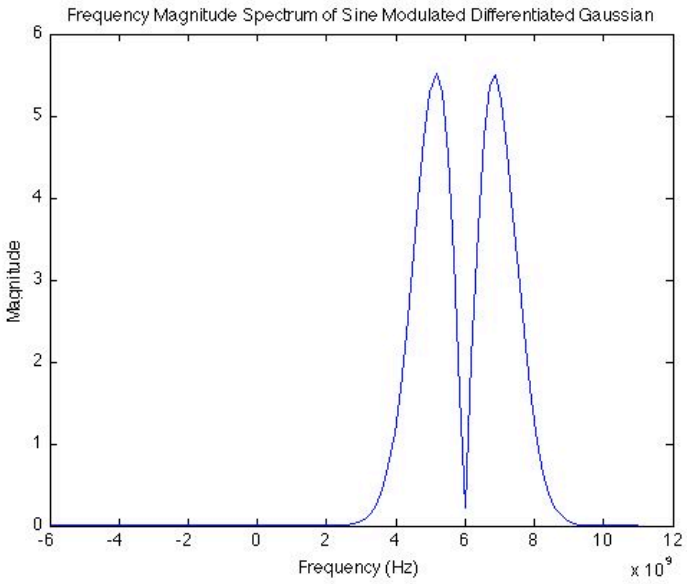

Figure 24: Frequency magnitude spectrum of input signal generated using MATLAB. The frequency range is 3 GHz to 9 GHz

The input signal is imported into the AWG in ".txt" format and sampled at 20 Gs/s. The signal as seen on the AWG can be seen in Figure 25. Figure 26 shows the resultant

input signal when the scope filters the high frequency components due to its limited sampling rate. This results in a smooth signal, which is the desired one.

Figure 25: Input signal as seen on the AWG sampled at 20 Gs/s

Figure 26: Input signal transmitted using a wire to the scope. The filtering of the high frequency components in the scope results in a smooth input signal as required.

Figure 27 shows the input signal when transmitted through the antennas as both antenna apertures are touching. This determined any changes in the signals caused by the antennas themselves rather than by any medium between them. Two 12 dB amplifiers are connected between the output of the AWG and the input of the transmit anetnna in order to amplify the input signal and make up for losses caused by the phantoms in order to be able to obtain measurable results. This input signal was determined to be suffiecient for

this application since the original shape was properly restored and transmitted via the antennas.

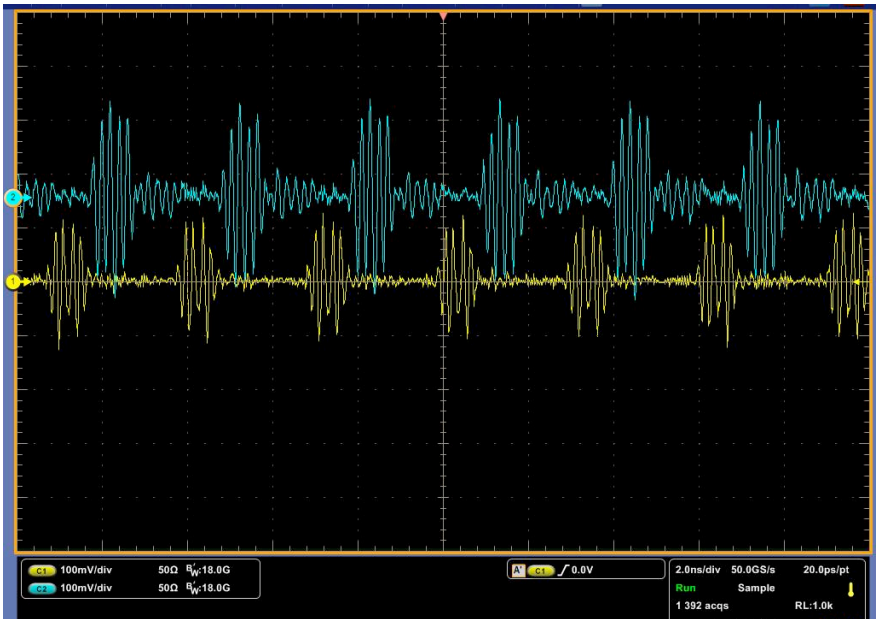

Figure 27: Input signal transmitted through a wire in yellow and input signal as transmitted by the antenna in blue (measured when both antenna apertures are touching).

5.3 Experimental Setup Using the VNA

The general setup of the experiment using the VNA is the same as that using the AWG and the scope as seen in Figure 28. Two amplifiers are again used. Since there measurements are performed using the time-domain option of a VNA, there was the option of choosing to record S_{11} or S_{12} signals. However, S_{11} measurements do not result in a distinguishable tumor signature and thus S_{12} is used to report all the data.

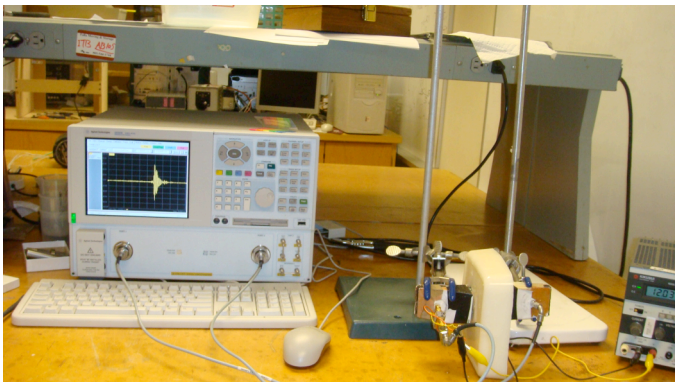

Figure 28: Experimental setup using the VNA.

The input signal is provided by the VNA and is a sine modulated Gaussian pulse in the frequency range of 3 GHz to 9 GHz as seen in Figure 29. Figure 30 shows the effect of the antennas on the input signal.

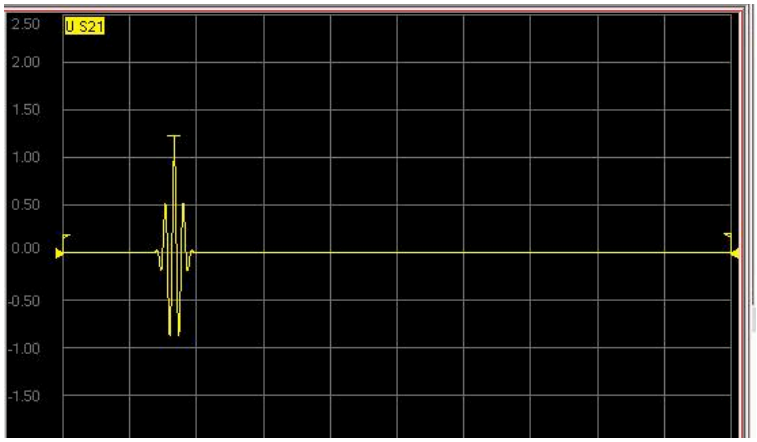

Figure 29: Sine modulated Gaussian input signal using the VNA.

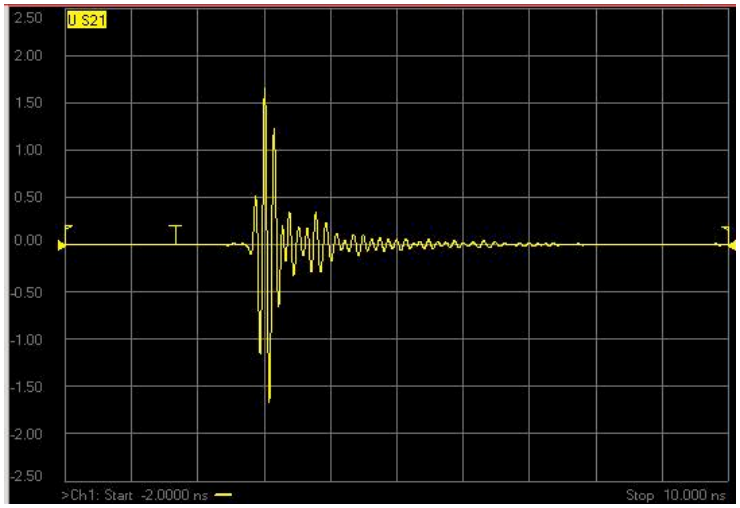

Figure 30: Input signal as transmitted by the antenna (measured when both antenna apertures are touching).

5.4 Data Processing

A similar algorithm to that used to process the signals recorded in simulations is used to process the measurement results in which the integration of the difference between tumor and no tumor recorded signals is computed at every point. However, measurements are performed only at three points rather than in a continuous manner as in simulations (due to the difficulty of moving the phantom). The first point in right at the

center of the tumor, the send is with the antenna covering around half of the tumor and one with the antenna away from the tumor.

6. Results and Discussion

6.1 Simulation Results

Simulation results were obtained for various situations: one tumor of diameter 6mm, 3 mm and 1 mm; two tumors of diameter 3 mm at a separation of 5 mm and of 5mm at a separation of 5 mm and 7 mm. Only sample results for the 6 mm diameter tumor are shown in detail. For all other cases, only the final result is shown, as the intermediate steps are the same. The simulation results were obtained using by processing the saved voltage waveform at different excitation-probe locations. Since a lot of results were obtained, Figure 31 and Figure 32 show sample recorded time-domain voltage waveforms for select x positions in the presence of one 6 mm diameter tumor and two 5 mm diameter tumors 5 mm apart, respectively. As seen in the figures, the maximum difference between recorded signals is at $x = 0$ at the center of the tumor. This difference decreases the further away the x position is from the tumor, to become almost zero at $x =$ 20 mm.

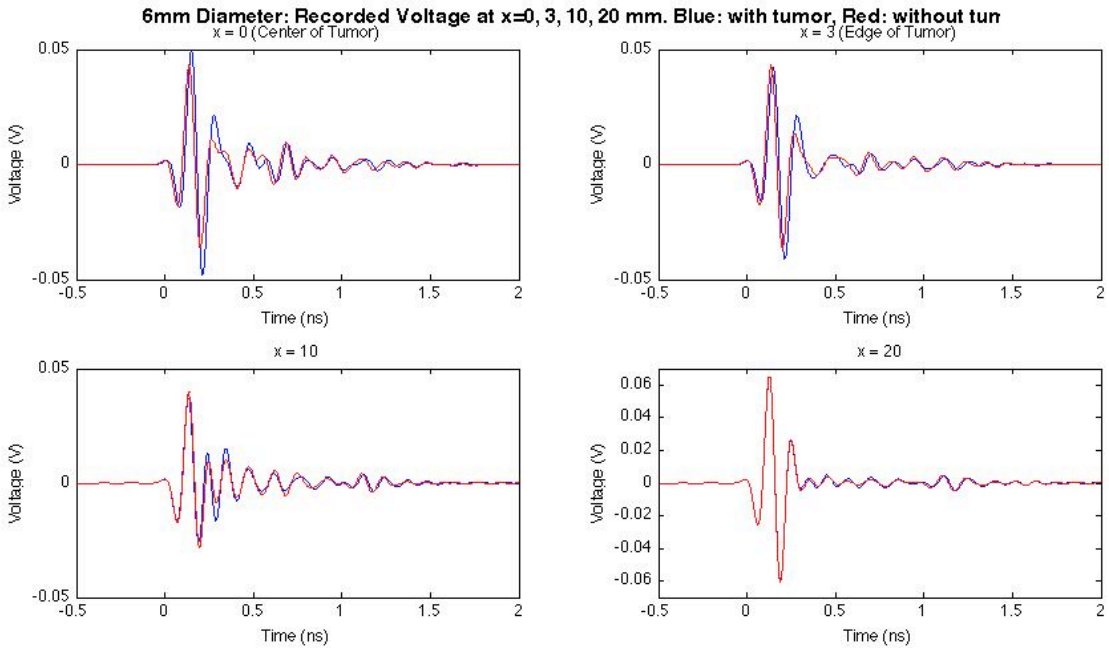

Figure 31: Recorded time-domain voltage waveforms for simulation with one 6 mm diameter tumor.

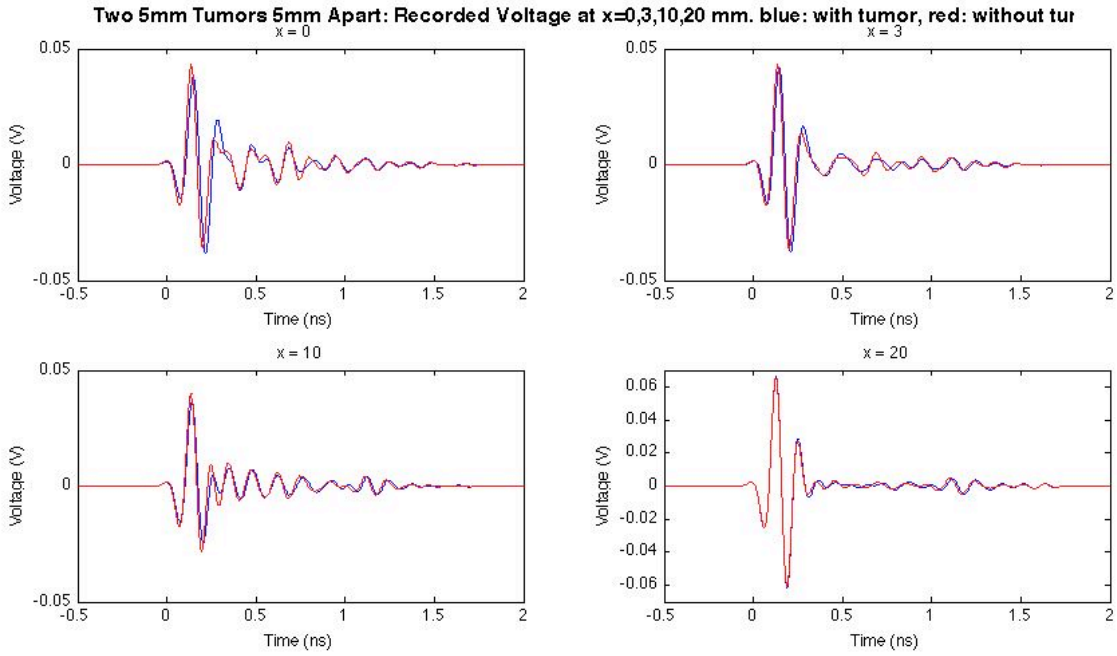

Figure 32: Recorded time-domain voltage waveforms for simulation with two 5 mm diameter tumors 5mm apart.

The image formation process, as mentioned earlier in this report in the "Image Formation" section of the simulation setup, is applied to all the recorded signals that are mostly similar to those seen in Figure 31 and Figure 32. Sample results for 6 mm diameter tumor is shown in Figure 33, Figure 34, Figure 35, and Figure 36. The 1D plot of the calculated intensities as a function of *x* position shows that a maximum is present at the center of the tumor, with the tumor signature decreasing the further away the scanning point is from its center. Since this is the plot that clearly shows the results, further results will only be shown in the 1D plot to be analyzed and discussed.

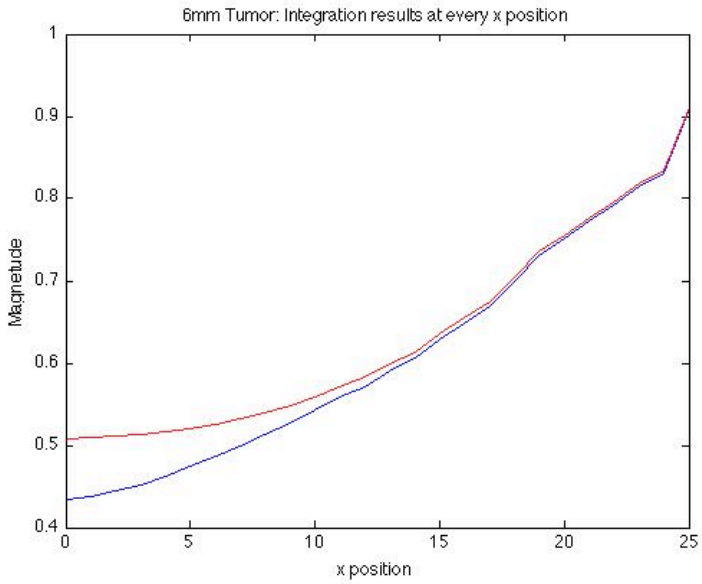

Figure 33: Sample integration results at every *x* position for one 6 mm tumor. Blue: with tumor, Red: without tumor.

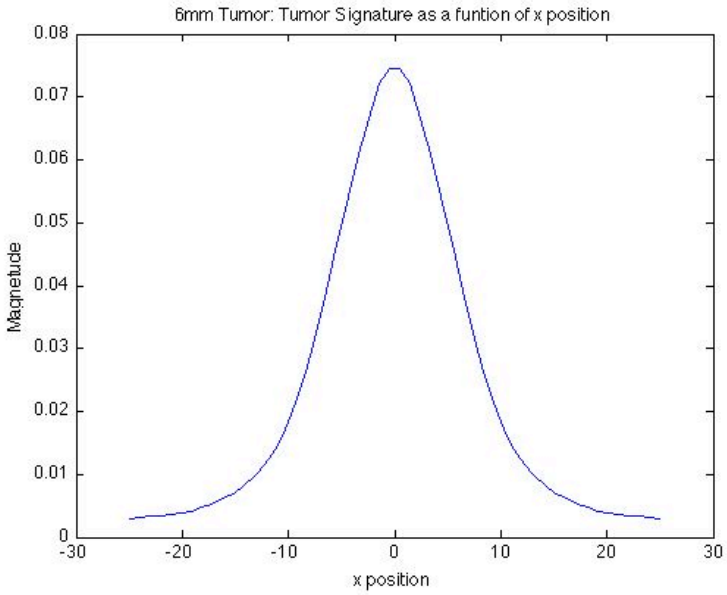

Figure 34: 6 mm diameter tumor: difference between integration results of signal with tumor and signal without tumor in 1D along the *x* direction.

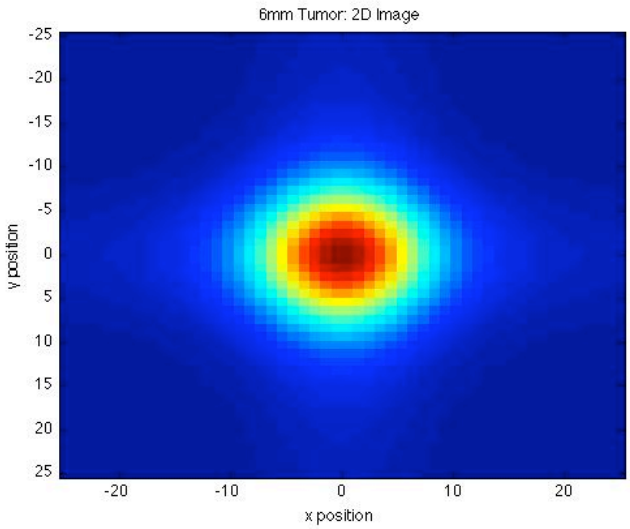

Figure 35: Sample 2D intensities in the *x* and *y* directions for one 6 mm diameter tumor.

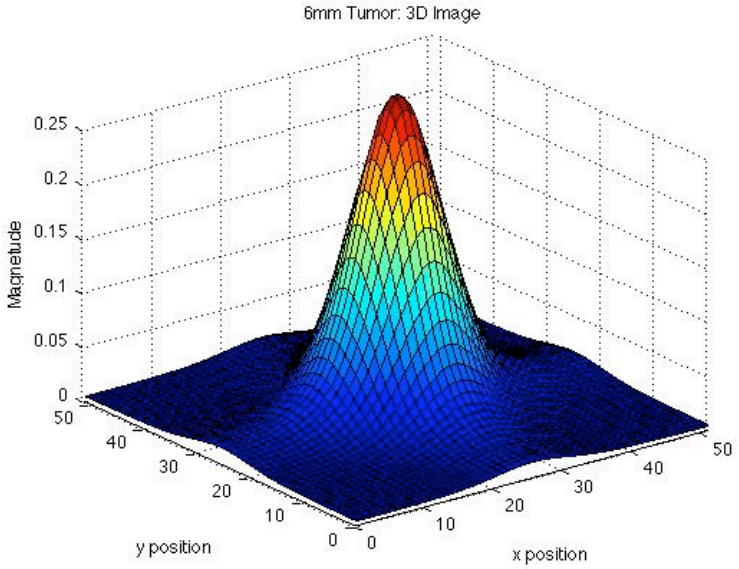

Figure 36: Sample 3D view of the resulting image of one 6 mm diameter tumor.

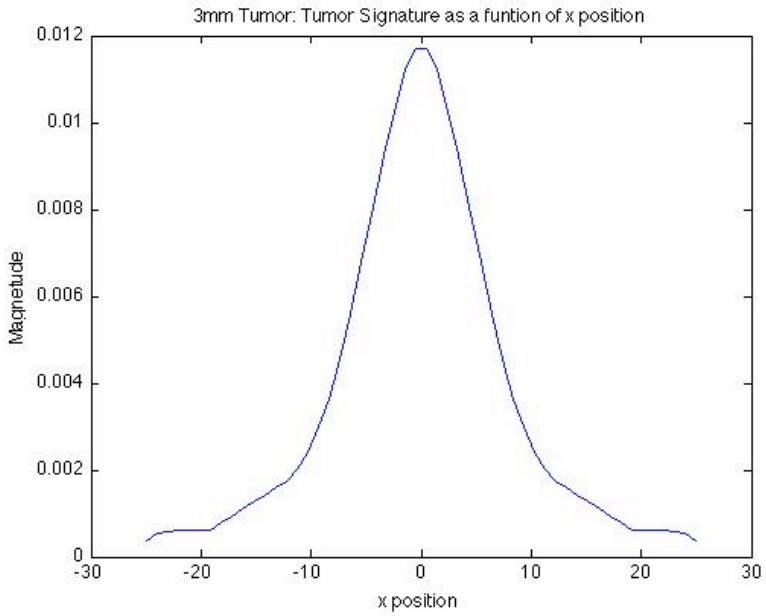

Figure 37: 3 mm diameter tumor: difference between integration results of signal with tumor and signal without tumor in 1D along the x direction.

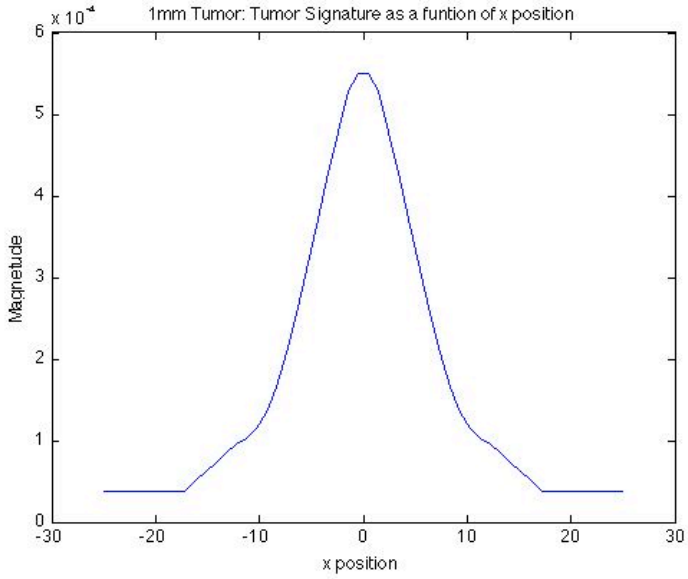

Figure 38: 1 mm diameter tumor: difference between integration results of signal with tumor and signal without tumor in 1D along the x direction.

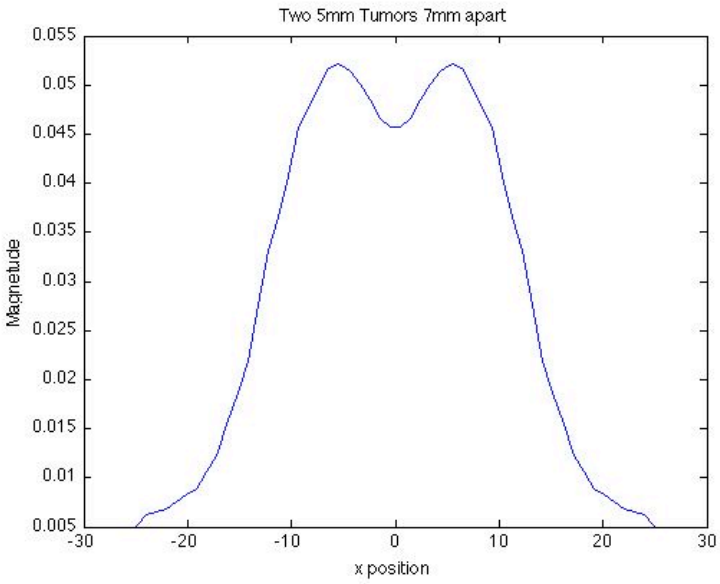

Figure 39: Two 5 mm tumors 7 mm apart: difference between integration results of signal with tumor and signal without tumor in 1D along the x direction.

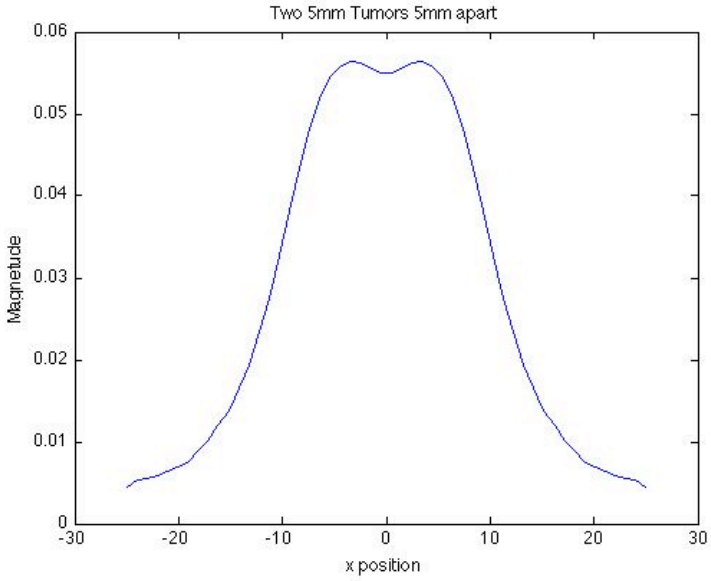

Figure 40: Two 5 mm tumors 5 mm apart: difference between integration results of signal with tumor and signal without tumor in 1D along the x direction.

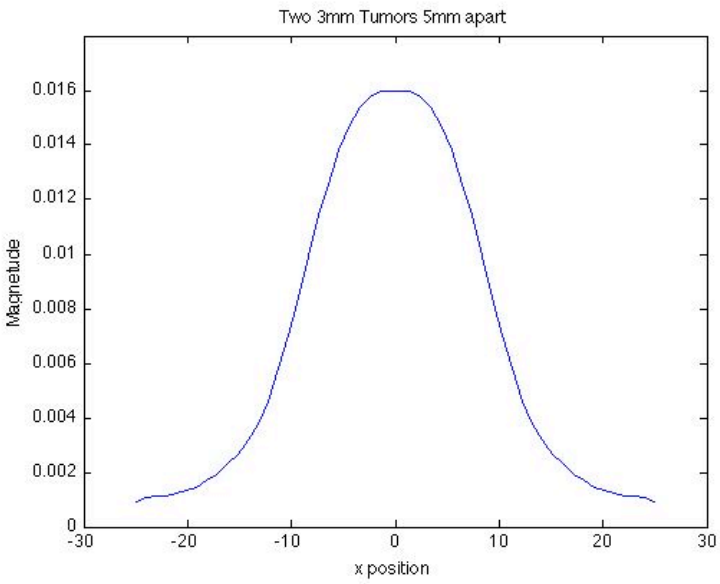

Figure 41: Two 3 mm tumors 5 mm apart: difference between integration results of signal with tumor and signal without tumor in 1D along the x direction.

As seen from the results presented in Figure 34, Figure 37, Figure 38, Figure 39, Figure 40, and Figure 41, the peak difference is always at the center of tumor, even in the presence of two tumors, two separate peaks are visible up to a certain limit. Also, as the results demonstrate, detecting two tumors does not only depend on their separation but also on their sizes. The sizes of the tumors only seem to affect the magnitude of the difference rather than its width. The 6 mm diameter tumor resulted in a peak that is around 0.075 V, while the 3 mm tumor resulted in a peak that is around 0.012 V and 1 mm resulted in a peak that is in the order of 0.1 mV. This is one of the reasons behind which small tumors are hardly detected in measurements because this difference is buried in the noise. In the case with two 3 mm tumors 5 mm apart, only one peak is visible, however, this peak appears broader than the peaks with one tumor, thus signaling the presence of two tumors, since it was determined that the diameter of the tumor only affects the height of the peak rather than its width.

6.2 Experimental Results Using the AWG and the Scope

Figure 42, Figure 43, Figure 44, Figure 45, Figure 46, Figure 47, and Figure 48 show the results of measurements performed using the scope. Figure 42 shows the attenuation

caused by placing a LWCT phantom between the antennas. Figure 43 and Figure 46 show the signal received without the presence of a tumor. Figure 44 shows the signal received at the center of a tumor in the LCWT phantom. The tumor signature is clearly visible when comparing those plots, as the tumor signal is almost completely attenuated by the presence of the very lossy tumor. Figure 48 shows the result of applying the same algorithm used on simulation results to the results obtained from this experiment. Again, the peak difference is at the center of the tumor.

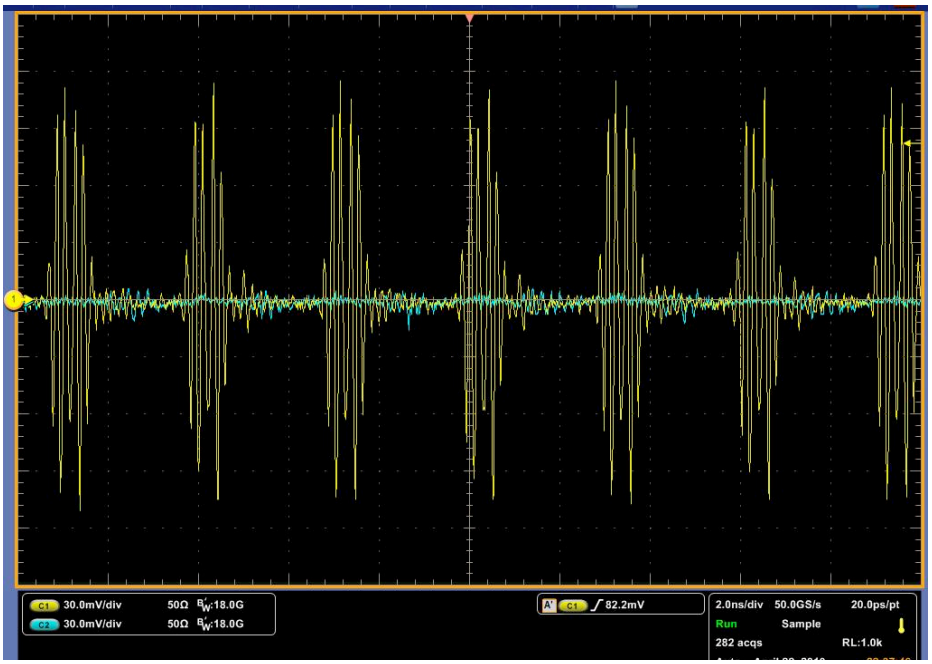

Figure 42: Transmitted signal recorded at the center of a LWCT phantom with no tumor using the scope in blue compared to the actual input signal to show the attenuation caused by the 3.5 cm thick LWCT phantom.

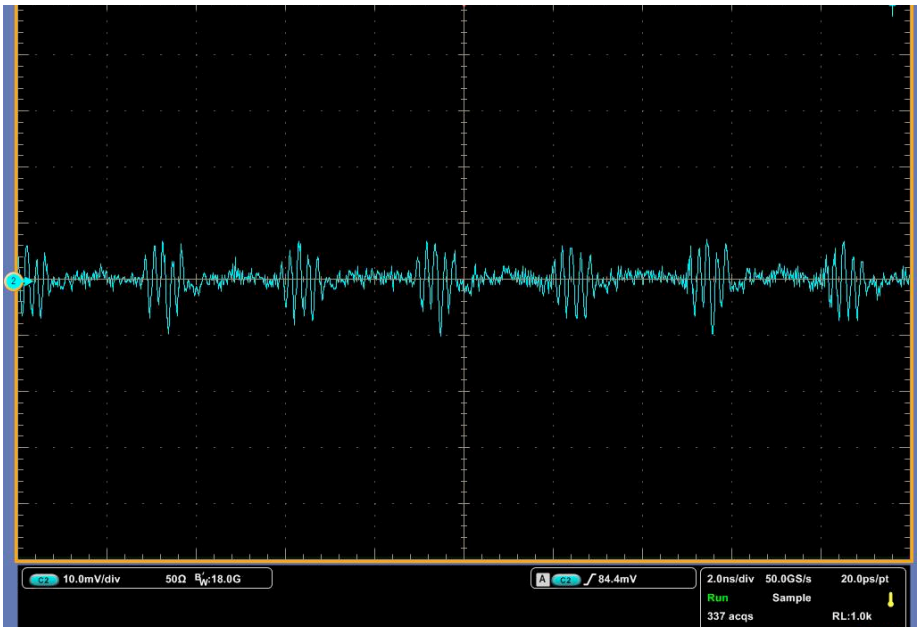

Figure 43: Transmitted signal recorded at the center of a LWCT phantom with no tumor using the scope.

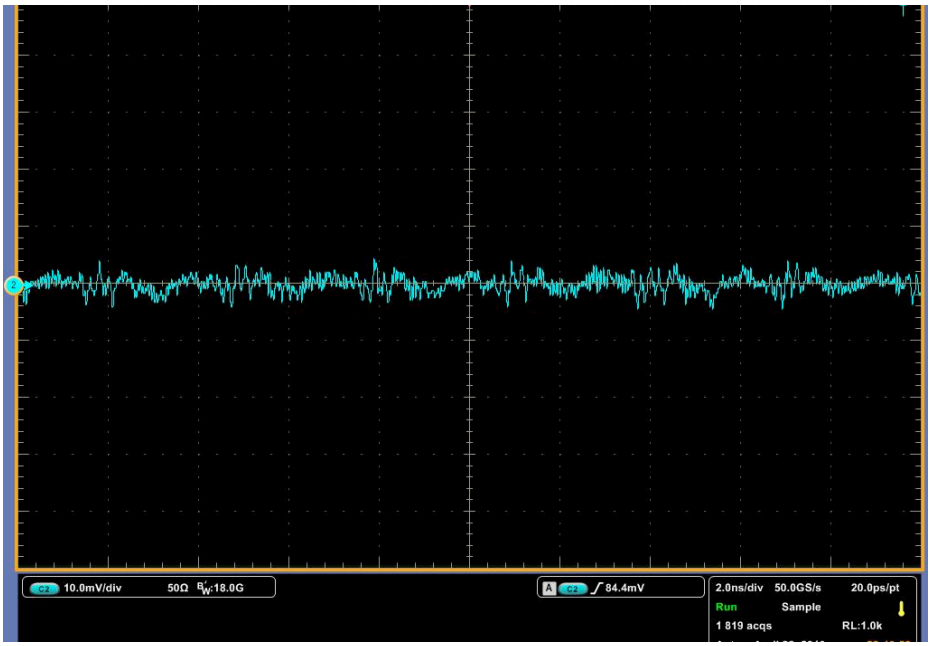

Figure 44: Transmitted signal recorded at the center of a tumor embedded in a LWCT phantom with the same properties of that with no tumor.

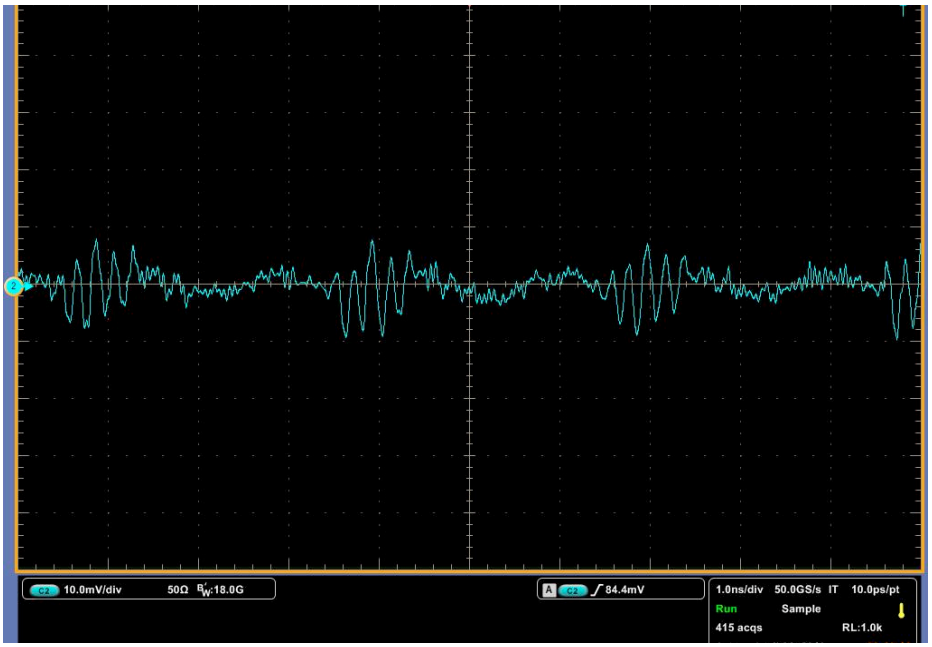

Figure 45: Transmitted signal recorded with the antenna covering half the tumor embedded in a LWCT phantom with the same properties of that with no tumor.

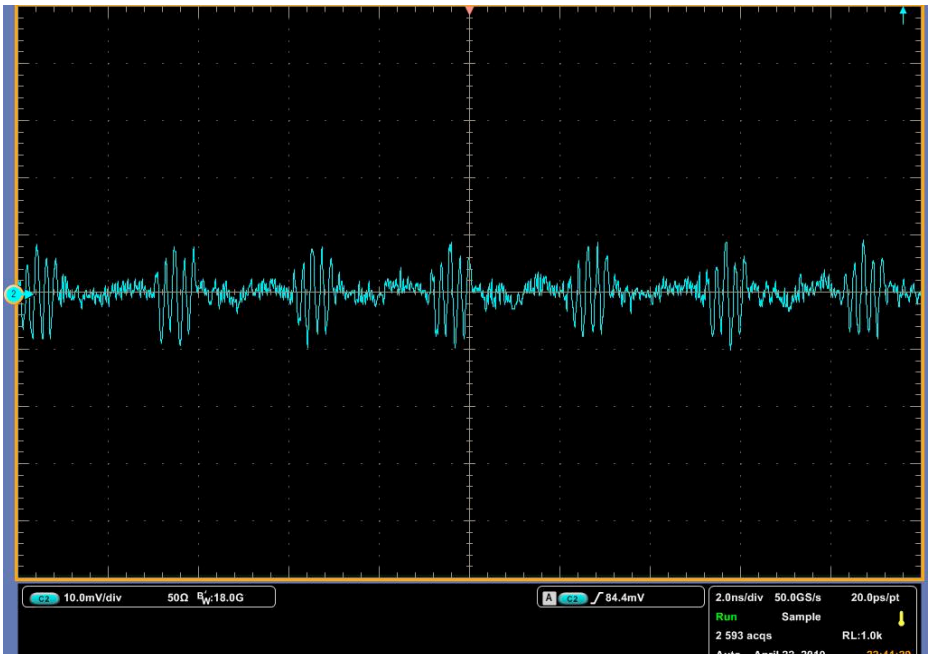

Figure 46: Transmitted signal recorded away from the tumor that is embedded in a LWCT phantom with the same properties of that with no tumor.

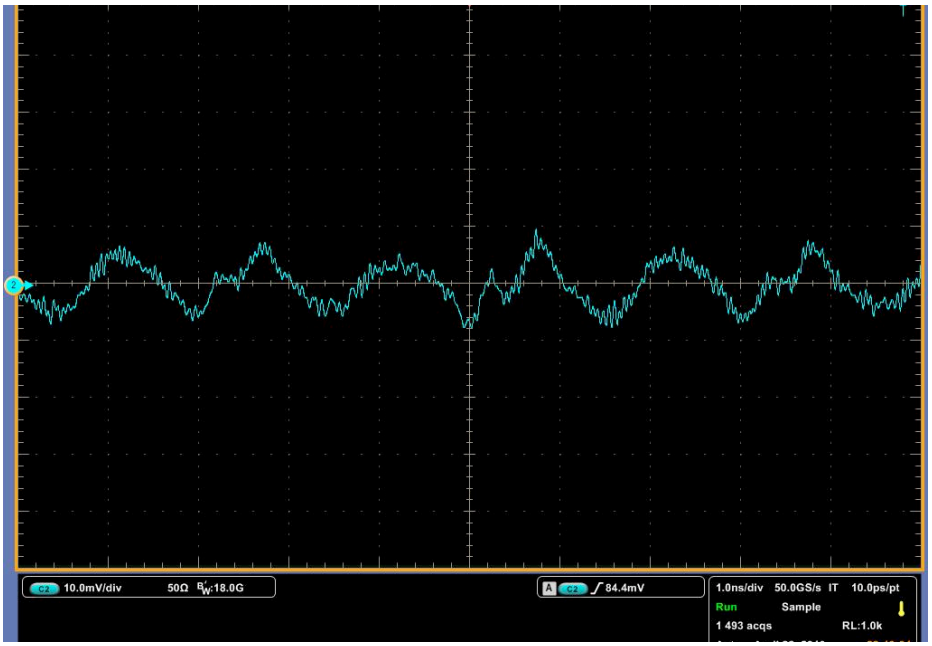

Figure 47: Transmitted signal recorded at the center of a 2.5 thick HWCT phantom with no tumor using the scope. This demonstrates that HWCT phantoms gravely distort and attenuate the input signal making it difficult to use in measurements.

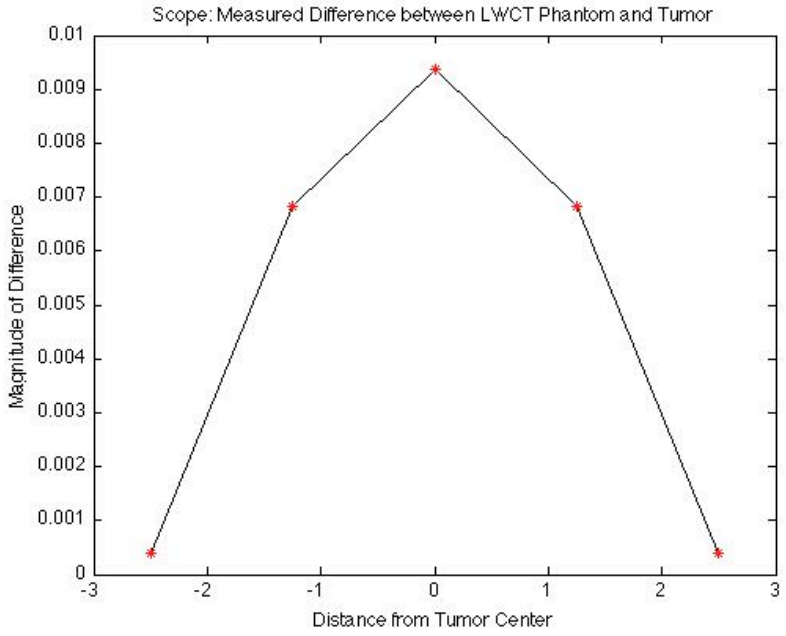

Figure 48: Measured difference between tumor and no tumor for a LWCT phantom using the scope.

6.3 Experimental Results Using the VNA

Figure 49, Figure 50, and Figure 51 show the results of measurements performed using the VNA. Figure 49 shows the signal without tumor (red) and at the center of a tumor (yellow) in the LCWT phantom. The tumor signature is clearly visible when comparing those plots, as the tumor signal is much more attenuated by the presence of the very lossy medium. Figure 50 shows the result of applying the same algorithm used on simulation results to the results obtained from this experiment. Again, the peak difference is at the center of the tumor.

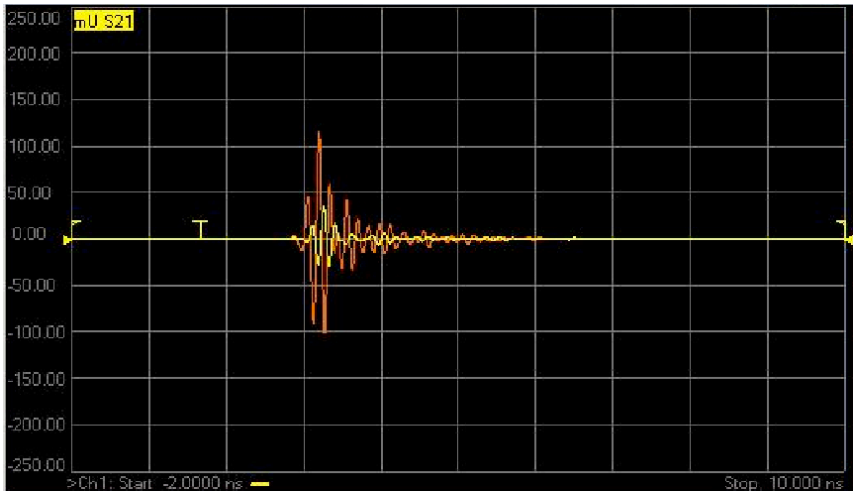

Figure 49: S_{21} measured using the VNA without the presence of a tumor in a LWCT phantom (red) and at the center of a tumor in the same phantom (yellow).

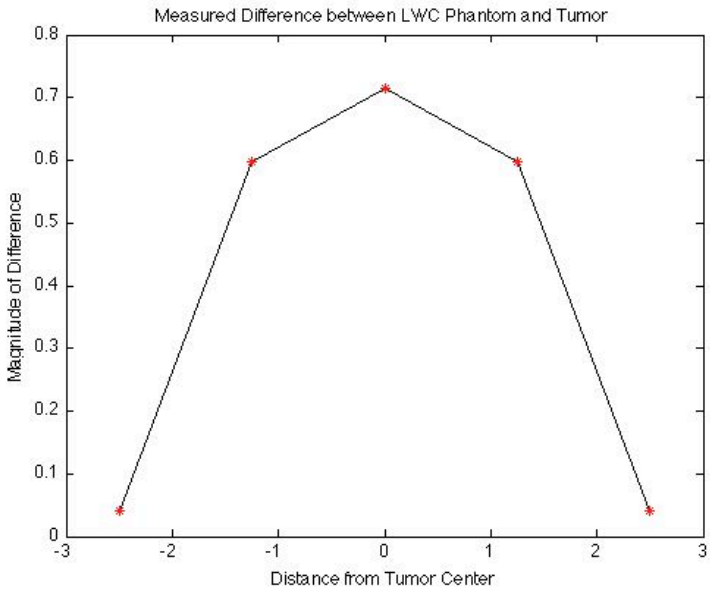

Figure 50: Measured difference between tumor and no tumor for a LWCT phantom using the VNA.

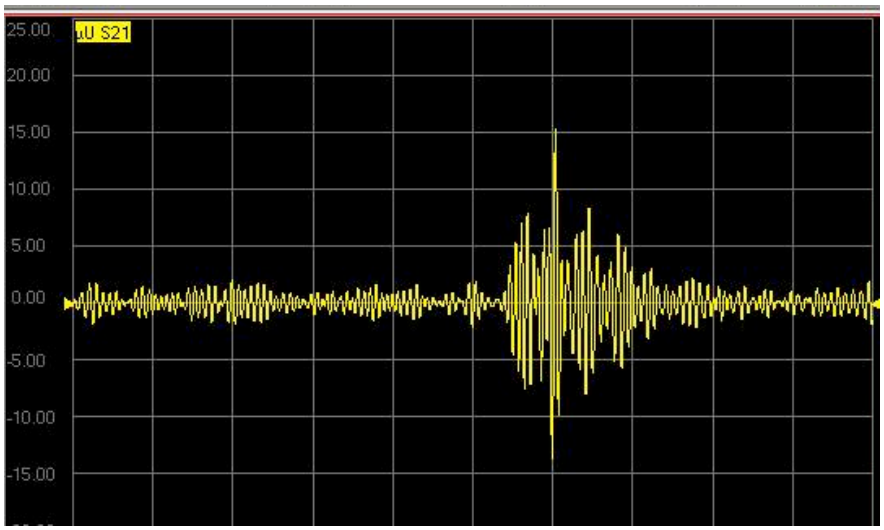

Figure 51: S_{21} measured using the VNA using a HWCT. The signal is mostly noise, being in the order of microvolts.

7. CONCLUSIONS AND RECOMMENDATIONS

In this report primary work has been presented to determine the effectiveness of time-domain measurements to detect breast cancers using microwave imaging. It has been shown that this technique can in fact be used to localize tumors in adipose tissue even through the use of a simple subtraction algorithm. This was concluded upon the use of three ways to test the system. Time-domain simulations, direct time-domain

measurements and synthesized time-domain measurements of the same setup yielded very similar and promising results. A wide range of future work should be performed in order to determine the functionality of this system in different other situations. Firstly, a study should be performed to determine whether time-domain measurements do, in fact, result in most accurate results when compared to frequency domain measurements. Also, more work needs to be done to test this system using the other various types of tissue found in the breast rather than only fat and muscle. Thus the sensitivity of this system to different tissue-tumor contrasts can be determined. Moreover, further studies should be conducted using the more complex algorithms similar to those presented in some of the literature reviewed in this report. Overall, small steps ought to be taken towards performing measurements on real breasts in the hope of allowing microwave imaging to replace the more conventional breast imaging modalities, thus offering lower cost, more patient comfort and minimum health risks as well as accurate tumor detection.

Appendix I : Recipe Ratios of Different Phantoms

Materials	Weight % Based on Glycerine
Glycerine	100
DIW	180
PEP	15
Agar	12

Table 3: Recipe ratio for HWCT-1

Materials	Weight % Based on Glycerine
Glycerine	100
DIW	140
PEP	14
Agar	11

Table 4: Recipe ratio for HWCT-2

Materials	Weight % Based on Glycerine
Glycerine	100
DWI	100
PEP	8
Agar	8

Table 5: Recipe ratio for IWCT

Materials	Weight % Based on Glycerine
Glycerine	100
DIW	8
Ethylene Glycol	52
PEP	10
Agar	11.5

Table 6: Recipe ratio for LWCT

Materials	Quantity
Alginate Powder	18 g [changed to 23 g]
DIW	100 g
NaCl	0.7 g

Table 7: Recipe ratio for Malignant-1

Source: [16]

Appendix II : MATLAB Code

A. Sample MATLAB Code Used to Process Simulation Results

```
%%Load files%%
load ('NOtumorx0_INF.txt');
load ('NOtumorx1_INF.txt');
load ('NOtumorx2_INF.txt');
load ('NOtumorx3_INF.txt');
load ('NOtumorx4_INF.txt');
load ('NOtumorx5_INF.txt');
load ('NOtumorx5_INF.txt');
load ('NOtumorx6_INF.txt');
load ('NOtumorx6_INF.txt');
load ('NOtumorx7_INF.txt');
load ('NOtumorx8_INF.txt');
load ('NOtumorx9_INF.txt');
load ('NOtumorx10_INF.txt');
load ('NOtumorx11_INF.txt');
load ('NOtumorx12_INF.txt');
load ('NOtumorx13_INF.txt');
load ('NOtumorx15_INF.txt');
load ('NOtumorx17_INF.txt');
load ('NOtumorx20_INF.txt');
load ('NOtumorx25_INF.txt');
load ('tumorx0_6MM.txt');
load ('tumorx1_6MM.txt');
load ('tumorx2_6MM.txt');
load ('tumorx3_6MM.txt');
load ('tumorx4_6MM.txt');
load ('tumorx5_6MM.txt');
load ('tumorx5_6MM1.txt');
load ('tumorx6_6MM.txt');
load ('tumorx6_6MM2.txt');
load ('tumorx7_6MM.txt');
load ('tumorx7_6MM2.txt');
load ('tumorx8_6MM.txt');
load ('tumorx9_6MM.txt');
load ('tumorx10_6MM.txt');
load ('tumorx11_6MM.txt');
load ('tumorx12_6MM.txt');
load ('tumorx13_6MM.txt');
load ('tumorx15_6MM.txt');
load ('tumorx17_6MM.txt');
load ('tumorx20_6MM.txt');
load ('tumorx25_6MM.txt');
```

```
%%Save necessary 6mmormation to be used%%
T0=tumorx0_6MM(:,3);
T1=tumorx1_6MM(:,3);
T2=tumorx2_6MM(:,3);
T3=tumorx3_6MM(:,3);
T4=tumorx4_6MM(:,3);
T5=tumorx5_6MM1(:,3);
T6=tumorx6_6MM2(:,3);
T7=tumorx7_6MM2(:,3);
T8=tumorx8_6MM(:,3);
T9=tumorx9_6MM(:,3);
T10=tumorx10_6MM(:,3);
T11=tumorx11_6MM(:,3);
T12=tumorx12_6MM(:,3);
T13=tumorx13_6MM(:,3);
T15=tumorx15_6MM(:,3);
T17=tumorx17_6MM(:,3);
T20=tumorx20_6MM(:,3);
T25=tumorx25_6MM(:,3);

NT0=NOtumorx0_INF(:,3);
NT1=NOtumorx1_INF(:,3);
NT2=NOtumorx2_INF(:,3);
NT3=NOtumorx3_INF(:,3);
NT4=NOtumorx4_INF(:,3);
NT5=NOtumorx5_INF(:,3);
NT6=NOtumorx6_INF(:,3);
NT7=NOtumorx7_INF(:,3);
NT8=NOtumorx8_INF(:,3);
NT9=NOtumorx9_INF(:,3);
NT10=NOtumorx10_INF(:,3);
NT11=NOtumorx11_INF(:,3);
NT12=NOtumorx12_INF(:,3);
NT13=NOtumorx13_INF(:,3);
NT15=NOtumorx15_INF(:,3);
NT17=NOtumorx17_INF(:,3);
NT20=NOtumorx20_INF(:,3);
NT25=NOtumorx25_INF(:,3);

%%Integrate the recorded signals at every point in the
presence of a tumor
len = length(T0);
Tumor = zeros(26,1);

for i=1:len
    Tumor(1,1)= Tumor(1,1) + (T0(i));
    Tumor(2,1)= Tumor(2,1) + (T1(i));
```

```
    Tumor(3,1)= Tumor(3,1) + (T2(i));
    Tumor(4,1)= Tumor(4,1) + (T3(i));
    Tumor(5,1)= Tumor(5,1) + (T4(i));
    Tumor(6,1)= Tumor(6,1) + (T5(i));
    Tumor(7,1)= Tumor(7,1) + (T6(i));
    Tumor(8,1)= Tumor(8,1) + (T7(i));
    Tumor(9,1)= Tumor(9,1) + (T8(i));
    Tumor(10,1)= Tumor(10,1) + (T9(i));
    Tumor(11,1)= Tumor(11,1) + (T10(i));
    Tumor(12,1)= Tumor(12,1) + (T11(i));
    Tumor(13,1)= Tumor(13,1) + (T12(i));
    Tumor(14,1)= Tumor(14,1) + (T13(i));
    Tumor(16,1)= Tumor(16,1) + (T15(i));
    Tumor(18,1)= Tumor(18,1) + (T17(i));
    Tumor(21,1)= Tumor(21,1) + (T20(i));
    Tumor(26,1)= Tumor(26,1) + (T25(i));
end

%%Allocate the value of the previous point (in the negative
x direction) to
%%the points with no corresponding data%%
for j=2:length(Tumor)
    if Tumor(j,1) == 0
        Tumor(j,1) = Tumor((j-1),1);
    end
end

Smooth_Tumor = smooth(Tumor);
x = linspace(0,25,26);

%%Plot the integration result of every signal as a function
of x position
%%with tumor%%
figure, plot (x, Smooth_Tumor);
title '6mm Tumor: Integration results at every x position';
hold;

%%Integrate the recorded signals at every point with no
tumor
lenNT = length(NT0);
NOTumor = zeros(26,1);

for i=1:lenNT
    NOTumor(1,1)= NOTumor(1,1) + (NT0(i));
    NOTumor(2,1)= NOTumor(2,1) + (NT1(i));
    NOTumor(3,1)= NOTumor(3,1) + (NT2(i));
    NOTumor(4,1)= NOTumor(4,1) + (NT3(i));
    NOTumor(5,1)= NOTumor(5,1) + (NT4(i));
```

```
    NOTumor(6,1)= NOTumor(6,1) + (NT5(i));
    NOTumor(7,1)= NOTumor(7,1) + (NT6(i));
    NOTumor(8,1)= NOTumor(8,1) + (NT7(i));
    NOTumor(9,1)= NOTumor(9,1) + (NT8(i));
    NOTumor(10,1)= NOTumor(10,1) + (NT9(i));
    NOTumor(11,1)= NOTumor(11,1) + (NT10(i));
    NOTumor(12,1)= NOTumor(12,1) + (NT11(i));
    NOTumor(13,1)= NOTumor(13,1) + (NT12(i));
    NOTumor(14,1)= NOTumor(14,1) + (NT13(i));
    NOTumor(16,1)= NOTumor(16,1) + (NT15(i));
    NOTumor(18,1)= NOTumor(18,1) + (NT17(i));
    NOTumor(21,1)= NOTumor(21,1) + (NT20(i));
    NOTumor(26,1)= NOTumor(26,1) + (NT25(i));
end

%%Allocate the value of the previous point (in the negative
x direction) to
%%the points with no corresponding data%%
for j=2:length(NOTumor)
    if NOTumor(j,1) == 0
        NOTumor(j,1) = NOTumor((j-1),1);
    end
end

Smooth_NOTumor = smooth(NOTumor);

%%Plot the integration result of every signal as a function
of x position
%%without tumor%%
plot (x, Smooth_NOTumor,'r');
grid minor;

%%Calculate the difference between both integration
results%%
Difference = abs(Smooth_NOTumor - Smooth_Tumor);

%%Creating a 2D and 3D image of results using the symmetric
nature of%%
%%simulation geometry%%
picture = zeros (52,52);

for i=27:52
    for j=1:52
            picture (i,j) = Difference(i-26,1);
    end
end

Difference2 = zeros(26,1);
```

```
for i = 1:26

        Difference2(i,1) = Difference ((27-i),1);
end

for i=1:26
    for j=1:52
        picture (i,j) = Difference2(i,1);
    end
end

picture2 = zeros (52,52);

for i=27:52
    for j=1:52
           picture2 (j,i) = Difference(i-26,1);
    end
end

for i=1:26
    for j=1:52
        picture2 (j,i) = Difference2(i,1);
    end
end

Difference1 = [Difference2; Difference];


%%Plot resulting difference in 1D%%
xd = linspace(-25,25,52);
figure, plot (xd, Difference1);
title '6mm Tumor: Tumor Signature as a funtion of x
position';
grid minor;

%%Show 2D image (only for simulations with one tumor)%%
x1 = linspace(-25,25,52);
picture3 = picture*picture2;
figure, imagesc(x1, x1, picture3);
title '6mm Tumor: 2D Image';
%%Show 3D image%%
figure;
subplot (2,2,1) , surf(picture3);
axis ([0 51 0 51 0 0.25]);
title '6mm Tumor: 3D Image';
```

B. MATLAB Code Used to Generate Input Signal for the AWG

```
t = 0e-9:0.05e-9:3e-9;
T = 190.52e-12;
to=5*T;
Vo = 5e9;

%%%%Original Differentiated Gaussian%%%%
V1 = (Vo*(t-to)).*exp((-(t-to).^2)./(T^2*2));
%%%Differentiated Gaussian with frequency shift%%%
V =(Vo*(t-to)).*exp((-(t-
to).^2)./(T^2*2)).*exp(2*pi*(6e9)*j.*t);
figure, plot (t, real(V));
title 'Sine Modulated Differentiated Gaussian';
xlabel ('Time (sec)');
ylabel ('Voltage (V)');

%%%Fourier%%%
f = linspace(-6e9,11e9,100);
VF = zeros(1,length(f));

for i=1:length(f)
    for k=1:length(V)
        VF(i) = VF(i) + V(k)*exp(-j*2*pi*f(i)*t(k));
    end
end

figure, plot (f, abs(VF));
title 'Frequency Magnitude Spectrum of Sine Modulated
Differentiated Gaussian';
xlabel ('Frequency (Hz)');
ylabel ('Magnitude');

%open the file with write permission
fid = fopen('gaussian_FINAL_3_9GHz.txt', 'w');
fprintf(fid,'%f\n', V);
fclose(fid);
load gaussian_FINAL_3_9GHz.txt;     %  read data
%  Plot data in text file to check
figure, plot (gaussian_FINAL_3_9GHz(:,1));
```

Appendix III : Tables of Measured ε'(ω) and ε"(ω) of Different Phantoms

LWCT

Frequency	ε'(ω)	ε"(ω)
3000000000	6.9544	4.5744
3140000000	6.7893	4.3793
3280000000	6.7236	4.2601
3420000000	6.6947	4.0955
3560000000	6.5957	3.9808
3700000000	6.6346	3.8965
3840000000	6.4876	3.7317
3980000000	6.4135	3.5784
4120000000	6.3593	3.4956
4260000000	6.2935	3.4097
4400000000	6.3181	3.3132
4540000000	6.2654	3.2499
4680000000	6.137	3.1386
4820000000	6.1495	3.0413
4960000000	6.091	2.9497
5100000000	6.0936	2.8923
5240000000	6.116	2.8592
5380000000	5.9899	2.7676
5520000000	5.9852	2.7126
5660000000	5.9571	2.6175
5800000000	5.9185	2.5525
5940000000	5.9686	2.5215
6080000000	5.8911	2.4611
6220000000	5.8196	2.3865
6360000000	5.8705	2.3478
6500000000	5.7924	2.2917
6640000000	5.811	2.2988
6780000000	5.8797	2.2463
6920000000	5.7204	2.1494
7060000000	5.6096	2.1321
7200000000	5.7419	2.1017
7340000000	5.7911	2.0523
7480000000	5.6757	2.0342
7620000000	5.6356	2.0347
7760000000	5.6619	1.9603
7900000000	5.5852	1.9101
8040000000	5.6005	1.8732
8180000000	5.6612	1.8795
8320000000	5.666	1.8369
8460000000	5.5623	1.7885

8600000000	5.4785	1.7175
8740000000	5.5566	1.742
8880000000	5.5974	1.7838
9020000000	5.5898	1.6728
9160000000	5.4945	1.6075
9300000000	5.4336	1.6332
9440000000	5.4441	1.6399
9580000000	5.6092	1.5251
9720000000	5.4435	1.6334
9860000000	5.5319	1.6149
10000000000	5.437	1.443

Table 8: LWCT phantom measured properties

HWCT

Frequency	$\varepsilon'(\omega)$	$\varepsilon''(\omega)$
3000000000	82.9226	1.6898
3140000000	83.131	1.6705
3280000000	83.2032	1.7656
3420000000	83.2744	1.8278
3560000000	83.3189	1.8681
3700000000	83.4032	1.8997
3840000000	83.6761	1.8018
3980000000	83.7693	1.8078
4120000000	83.8712	1.7998
4260000000	83.9804	1.7948
4400000000	84.1035	1.7444
4540000000	84.4655	1.4916
4680000000	84.5615	1.417
4820000000	84.8843	1.1812
4960000000	85.0046	1.0974
5100000000	85.0577	1.0503
5240000000	85.0984	1.0227
5380000000	85.1562	0.9189
5520000000	85.1324	0.8536
5660000000	85.0935	0.8182
5800000000	85.0308	0.804
5940000000	84.9731	0.7301
6080000000	85.0563	0.5219
6220000000	84.943	0.5697
6360000000	84.7878	0.5936
6500000000	84.6542	0.586
6640000000	84.4537	0.6401
6780000000	84.2446	0.7341
6920000000	83.9842	0.8273
7060000000	83.7256	0.905
7200000000	83.4807	1.025
7340000000	83.2229	1.1305

7480000000	82.9443	1.2349
7620000000	82.64	1.3908
7760000000	82.3318	1.4981
7900000000	82.062	1.6205
8040000000	81.7402	1.7188
8180000000	81.4266	1.8601
8320000000	81.1361	1.9696
8460000000	80.8202	2.0407
8600000000	80.5266	2.1666
8740000000	80.1843	2.3312
8880000000	79.9173	2.4146
9020000000	79.5189	2.471
9160000000	79.1957	2.7061
9300000000	78.8134	2.5184
9440000000	78.4585	2.8682
9580000000	78.1646	3.2058
9720000000	77.658	3.2266
9860000000	77.4884	3.3427
10000000000	77.1458	3.3428

Table 9: HWCT phantom measured properties

Tumor 1

Frequency	$\varepsilon'(\omega)$	$\varepsilon''(\omega)$
3000000000	51.9804	31.7768
3140000000	51.6149	31.4517
3280000000	51.2664	31.1433
3420000000	50.9404	30.9178
3560000000	50.5673	30.6997
3700000000	50.1973	30.5404
3840000000	49.8287	30.4221
3980000000	49.5031	30.3114
4120000000	49.1287	30.197
4260000000	48.7617	30.1663
4400000000	48.4377	30.1281
4540000000	48.1155	30.081
4680000000	47.7857	30.0821
4820000000	47.5476	30.0834
4960000000	47.211	30.1289
5100000000	46.8904	30.1832
5240000000	46.581	30.2459
5380000000	46.2805	30.3235
5520000000	45.986	30.3892
5660000000	45.722	30.5124
5800000000	45.4629	30.629
5940000000	45.2215	30.7554
6080000000	45.5092	31.024

6220000000	45.3557	31.1705
6360000000	45.2774	31.3723
6500000000	45.633	31.6841
6640000000	45.676	31.9035
6780000000	45.4255	32.0612
6920000000	45.025	32.145
7060000000	44.5782	32.2712
7200000000	44.2136	32.4115
7340000000	43.846	32.5331
7480000000	43.4557	32.6587
7620000000	43.1043	32.7721
7760000000	42.7359	32.8938
7900000000	42.3207	33.007
8040000000	41.9411	33.1432
8180000000	41.5665	33.2511
8320000000	41.1567	33.3677
8460000000	40.749	33.4581
8600000000	40.3396	33.571
8740000000	39.943	33.6837
8880000000	39.5168	33.7604
9020000000	39.1187	33.7952
9160000000	38.6537	33.8877
9300000000	38.2016	33.9718
9440000000	37.7814	34.0503
9580000000	37.3364	34.1048
9720000000	36.865	34.1189
9860000000	36.2977	34.0864
10000000000	35.7827	34.0975

Table 10: Tumor 1 phantom measured properties

Tumor 2

Frequency	$\varepsilon'(\omega)$	$\varepsilon''(\omega)$
3000000000	61.8273	23.0039
3140000000	59.891	22.2803
3280000000	59.1624	22.0281
3420000000	58.4723	21.8416
3560000000	57.8205	21.7388
3700000000	57.1654	21.5888
3840000000	56.2566	21.3543
3980000000	55.7303	21.3295
4120000000	55.2603	21.3505
4260000000	54.7907	21.3533
4400000000	54.3961	21.4061
4540000000	53.8329	21.3554
4680000000	53.4489	21.412
4820000000	52.9848	21.4571
4960000000	52.6466	21.5575

5100000000	52.3218	21.6439
5240000000	52.0001	21.7563
5380000000	51.651	21.8287
5520000000	51.3352	21.9255
5660000000	50.9973	22.038
5800000000	50.6665	22.1558
5940000000	50.3481	22.261
6080000000	49.9777	22.2866
6220000000	49.6632	22.3791
6360000000	49.3577	22.4786
6500000000	49.0469	22.5923
6640000000	48.7374	22.672
6780000000	48.4445	22.7397
6920000000	48.1282	22.8054
7060000000	47.8364	22.9019
7200000000	47.5788	23.0199
7340000000	47.2988	23.1131
7480000000	46.9975	23.1815
7620000000	46.7182	23.2859
7760000000	46.4322	23.3819
7900000000	46.149	23.511
8040000000	45.8686	23.6534
8180000000	45.6329	23.7366
8320000000	45.3435	23.8006
8460000000	45.0328	23.9232
8600000000	44.7535	24.0355
8740000000	44.463	24.1908
8880000000	44.1818	24.3058
9020000000	43.9094	24.3838
9160000000	43.5585	24.4542
9300000000	43.305	24.5753
9440000000	43.0877	24.7216
9580000000	42.8445	24.8878
9720000000	42.5546	25.0052
9860000000	42.2635	25.1614
10000000000	41.9942	25.3039

Table 11: Tumor 2 phantom measured properties

REFERENCES

[1] Canadian Cancer Society, *Canadian Cancer Statistics 2009*, pp. 15, 42,43 [Online]. http://www.cancer.ca/Canada-wide.aspx.

[2] E. C. Fear, X. Li, S. C. Hagness, and M. A. Stuchly, "Confocal microwave imaging for breast cancer detection: Localization of tumors in three dimensions," *IEEE Trans. Biomed. Eng.*, vol. 49, pp. 812–822, Aug. 2002.

[3] E. C. Fear, S. C. Hagness, P. M. Meaney, M. Okoniewski, and M. A. Stuchly, "Enhancing breast tumor detection with near field imaging," *IEEE Microwave Mag.*, vol.3, pp. 8–56, Mar 2002.

[4] S. C. Hagness, A. Taflove, and J. E. Bridges, "Two-dimensional FDTD analysis of a pulsed microwave confocal system for breast cancer detection: Fixed-focus and antenna-array sensors," *IEEE Trans. Biomed. Eng*., vol. 45, pp. 1470–1479, Dec. 1998.

[5] J. M. Sill, E. C. Fear, "Tissue Sensing Adaptive Radar for Breast Cancer Detection – Experimental Investigation of Simple Tumor Models," *IEEE Trans. Microwave Theory and Tech.,* vol. 53, no. 11, Nov. 2005.

[6] S. K. Davis, B. D. Van Veen, S. C. Hagness, F. Kelcz, "Breast Tumor Characterization Based on Ultrawideband Microwave Backscatter," *IEEE Trans. on Biomed. Eng.*, vol. 55, no. 1, Jan. 2008.

[7] M. Lazebnik, L. McCartney, D. Popovic, C. B. Watkins1, M. J. Lindstrom, J. Harter, S. Sewall, A. Magliocco, J. H. Booske, M. Okoniewski and S. C. Hagness, " A large – scale study of the ultra wideband microwave dielectric properties of normal breast tissue obtained from reduction surgeries*," Phys. Med. Biol.*, vol.52, pp.2637-2656, April 2007.

[8] M. Lazebnik, D. Popovic, L. McCartney, C. B. Watkins, M. J. Lindstrom, J. Harter, S. Sewall, T. Ogilvie, A. Magliocco, T. M. Breslin, W. Tempe, D. Mew, J. H. Booske, M. Okoniewski, and S. C. Hagness, "A large-scale study of the ultrawideband microwave dielectric properties of normal, benign, and malignant breast tissues obtained from cancer surgeries," *Phys. Med. Biol.*, vol. 52, pp. –6093–6115, Oct. 2007.

[9] E. C. Fear, J. Sill, and M. A. Stuchly, "Experimental feasibility study of confocal microwave imaging for breast tumor detection," *IEEE Trans. Microw. Theory Tech.*, vol. 51, no. 3, pp. 887–892, Mar. 2003.

[10] X. Li, E. J. Bond, B. D. Van Veen, and S. C. Hagness, "An overview of ultrawideband microwave imaging via space-time beamforming for early-stage breast cancer detection," *IEEE Antennas Propagat. Mag.*, vol. 47, no. 2, pp. 19–34, Feb. 2005.

[11] E. C. Fear and J. Sill, "Preliminary investigations of tissue sensing adaptive radar for breast tumour detection," *Proc. Engineering Medicine and Biology Society*, Cancun, Mexico, Sep. 2003, pp. 3787–3790.

[12] J. M. Sill and E. C. Fear, "Tissue sensing adaptive radar for breast cancer detection: Preliminary experimental results," *IEEE Int. Microwave Symp. Dig.,* 2005, 4, pp.1789-1792.

[13] R. K. Amineh, A. Trehan, and N. K. Nikolova, "TEM Horn antenna for ultra wideband microwave breast imaging," *Prog. in Electromag. Research B,"* vol.13, pp. 59-74, 2009.

[14] R. K. Amineh, M. Ravan, A. Trehan, and N. K. Nikolova,. *Ultra-Wide Band TEM Horn for Microwave Imaging Based on Aperture Scanning*. McMaster University, Ontario, Canada

[15] Sill, J. M. and E. C. Fear, "Tissue sensing adaptive radar for breast cancer detection: study of immersion liquids," *Electron. Lett.*, vol. 41, no. 3, pp. 113–115, 2005.

[16] A. Trehan. *Numerical and Physical Models for Microwave Breast Imaging*, Ch.3. M.A.Sc. Thesis, McMaster University, Ontario, Canada, 2009.

[17] Tektronix Inc., USA, http://www.tek.com.

[18] Agilent Technologies Inc., USA, http://www.**agilent**.com.

[19] Mini-Circuits ®, USA, http://www.minicircuits.com.

[20] QWED Sp., Poland, http://www.qwed.com.pl.

[21] A. Johnson, *Design of Ultra wideband Microwave Antenna Array for Detection of Breast Cancer Tumors,* EE 4BI6 Capstone, McMaster University, Ontario, Canada, 2009.

VITAE

Yona Baskharoun is currently a 4th year undergraduate student at McMaster University. She will complete her degree in May of 2010.